

CORRELATION BETWEEN THE
CRITICAL TEMPERATURE OF
CUPRATES SUPERCONDUCTORS AND
THEIR MAGNETIC INTERACTION

RINAT ASSA

**CORRELATION BETWEEN THE CRITICAL
TEMPERATURE OF CUPRATES
SUPERCONDUCTORS AND THEIR MAGNETIC
INTERACTION**

RESEARCH THESIS

**SUBMITTED IN PARTIAL FULFILLMENT OF THE
REQUIREMENTS FOR THE DEGREE OF MASTER OF
SCIENCE IN PHYSICS**

RINAT ASSA

**SUBMITTED TO THE SENATE OF THE TECHNION – ISRAEL INSTITUTE
OF TECHNOLOGY**

SIVAN, 5764

Haifa

May, 2004

THE RESEARCH THESIS WAS DONE UNDER THE SUPERVISION OF
PROF. AMIT KEREN IN THE FACULTY OF PHYSICS

I am deeply grateful for Prof. Amit Keren for the excellent guidance, for the support and encouragement.

I thank the lab technicians: Galina Bazalitsky, Dr. Leonid Iomin, and Larisa Patalgen for all their help.

Thank to all the friends in the research groupe: Oren, Eva, Oshri, Meni, Ariel, Lior, and a special thanks to Shahar and Amit for all their help.

THE GENEROUS FINANCIAL HELP OF THE TECHNION IS GRATEFULLY
ACKNOWLEDGED

To my parents, Daniel and Ady, for their unconditional love and support

And to Oren for everything

Contents

Abstract		ix
List of Symbols		1
1	PREFACE	3
2	MATERIALS – Structure and properties	7
2.1	YBCO.....	7
2.2	CLBLCO.....	9
3	REVIEW OF PERVIOUS RESULTS	11
3.1	The Uemura relations.....	11
3.2	Scaling relations.....	12
4	EXPERIMENTAL METHODS	15
4.1	Nuclear Quadrupole Resonance (NQR).....	15
4.1.1	FID (Free Induction Decay) and Spin echo.....	17
4.1.2	The experimental conditions.....	18
4.2	Muon Spin Relaxation (μ SR).....	19
4.2.1	Muon production, implantation and decay.....	19
4.2.2	Experimental setup.....	20
4.2.3	Muons in matter in Zero Field.....	23
4.3	Sample preparation.....	25
4.3.1	orientation.....	26
4.3.2	Enriched samples.....	26
5	RESULTS	27
5.1	NQR on YBCO.....	27
5.2	μ SR on CLBLCO.....	32

CONTENTS

6	DISCUSSION	35
6.1	NQR on YBCO.....	35
6.2	μ SR on CLBLCO.....	38
7	SUMMARY	41
A	The Derivation of the NQR Hamiltonian	43
	References	47

List of Figures

1.1	The main features of the cuprates phase diagram.....	4
2.1	Phase diagram of YBCO.....	8
2.2	The YBCO unit cell.....	8
2.3	The variation of T_c with oxygen doping in CLBLCO for various values of x . taken from [8].....	9
3.1	A Uemura plot showing T_c vs. the muon line width σ in a μ SR experiment for the CLBLCO, the LSCO and the YBCO families. σ is proportional to λ^{-2} which is proportional to n_g/m^* . λ is the magnetic penetration depth [3].....	12
3.2	(a) T_c/T_c^{max} and (b) T_g/T_c^{max} as a function of $\Delta p = K_f \Delta y$ for several HTSC families. K_f is chosen so that T_c/T_c^{max} vs. Δp of various cuprates families collapse into a single curve. As a consequence T_g/T_c^{max} vs. Δp also collapses into a single line.....	14
4.1	Different configurations of an oval shaped nucleus in a field of four charges. The configuration (b) is energetically favorable.....	15
4.2	A schematic description of a spin echo sequence. The two pulses are followed by a Gaussian shaped echo. The schematic polarization graphs are for spin 1/2 in NMR.....	18
4.3	The angular distribution of emitted positrons with respect to the initial muon-spin direction.....	20
4.4	Schematic illustration of a μ SR experiment.....	22
4.5	(a) the number of positrons detected in the forward and backward detectors. (b) The Asymmetry function. Taken from [9].....	23
4.6	Muon spin precession about the magnetic field at an angle θ	24
4.7	The Kubo-Toyabe polarization, the relaxation of the muon-spin due to Gaussian field distribution.....	25

LIST OF FIGURES

5.1	NQR frequency sweep on YBCO. The dotted line is the experimental result. The solid line is a Gaussian fit performed in order to determine the resonance frequencies.....	28
5.2	NQR frequency sweep for YBCO ₇ with both isotopes of copper. Instead of one resonance peak there is a Cu ⁶³ - Cu ⁶⁵ doublet.....	28
5.3	The intensity ratio between the 29MHz line and the 31MHz line as a function of the doping. As the doping decreases and oxygen is being removed from the chains the line of a Cu(2) with chain half full (29MHz) increases on the expense of Cu(2) with the chains full.....	29
5.4	The oxygen doping level in YBCO as a function of the NQR frequencies.....	30
5.5	Schematic illustration of the Cu site with locally different oxygen coordination.....	31
5.6	Asymmetry plots for varies temperatures for four CLBLCO samples	33
5.7	The magnetic amplitude Am as a function of temperature for a sample with $x=0.4$ and $y=6.607$	33
6.1	T_C for different YBCO samples as a function of the NQR frequencies. The solid lines are fits of the data to three lines with shared slope ($dT_C/df=38\pm 6$ (K/MHz)).....	36
6.2	T_C , Tg , and T_N as a function of the oxygen doping for four families of CLBLCO. The empty points are the superconducting transition temperature T_C , and the filed points are the magnetic transition temperatures Tg (in the spin glass phase), and T_N (in the antiferromagnetic phase).....	39
6.3	The superconducting transition temperature at optimal doping T_C^{max} as a function of the antiferromagnetic transition temperature T_N for the CLBLCO system.....	39

Abstract

Previous work in our group demonstrated that in the cuprates superconductors in the underdoped region: $T_C \propto J_f n_s$ where T_C is the superconductor transition temperature, J_f a magnetic energy scale for a given cuprates family, and n_s is the superconducting carrier density. But there is still no clear experimental confirmation that J_f is a constant for a given family, or of a correlation between the maximum transition temperature T_C^{max} and the Néel temperature T_N .

In the first part of this work I want to verify that the energy scale J_f is unique to each family for high temperature superconductors [HTSC], and is constant throughout all the doping range in the family. For this I perform NQR measurements, thus determining doping levels, on YBCO samples with various oxygen contents. I find that $T_C \propto n_s$ hence J_f must be a constant.

In the second part of this work I investigate the correlation between T_C^{max} and T_N (at very low doping) for a given family. For this purpose I used the CLBLCO families of superconductors and applied zero field muon spin relaxation measurements to determine both the spin glass and Néel transition temperatures T_g and T_N . This allows me to construct the phase diagram of the CLBLCO system. Using this phase diagram I show that the family with higher T_N indeed has the higher T_C^{max} .

The above results enhance our group previous experimental demonstration of a simple relation between magnetic energy scale, doping, and T_C .

List of Symbols

HTSC	High Temperature Superconductor
μ SR	Muon Spin Relaxation
NQR	Nuclear Quadruple Resonance
NMR	Nuclear Magnetic Resonance
EFG	Electron Field Gradient
T_C	Superconducting transition temperature
n_s	Superfluid density
m^*	Effective mass
J	Energy scale
p	doping level
T_C^{max}	T_C at the optimal doping point
T_N	Néel temperature
T_g	Spin glass transition temperature
x	Calcium level in CLBLCO
y	Oxygen level
y_0	Oxygen level at the optimal doping point
Δy	Oxygen level as measured from optimal doping
$K(x)$	Scaling constant of the doping
Δp	Scaled doping level
Cu(1)	Chain copper in YBCO
Cu(2)	Plane copper in YBCO
\hat{I}	Total angular momentum vector operators
η	Asymmetry parameter
$t_{\pi/2}$	Length of $\pi/2$ pulse
τ	Break time between pulses in a spin echo sequence
H_Q	Pure quadruple Hamiltonian

H_{rf}	Time dependent perturbation term of the Hamiltonian
γ	Gyromagnetic ratio
f	RF transmission frequency
f_{NQR}	Resonance frequency of the NQR Hamiltonian
B	Magnetic induction
$A(t)$	Muon asymmetry
N_B	Counts at the backward counter
N_F	Counts at the forward counter
T_2	Spin-spin relaxation time
T_1	Spin-lattice relaxation time
$G(t)$	Muon polarization
$\rho(B)$	Magnetic field distribution
$\rho(r)$	Charge density
$V_{\alpha\beta}$	The EFG tensor
l	Orbital angular momentum
Q	Quadrupole moment of a nucleus

Chapter 1

PREFACE

The cuprates high T_C superconductors are ceramic compounds all having CuO_2 planes. These compounds are antiferromagnetic Mott insulators in their undoped state. Upon holes or electrons doping, by replacing some of the out-of-plane atoms with atoms that prefer different oxidation states, they become High T_C superconductors [HTSC], and the long range antiferromagnetism is destroyed. The origin of the magnetism at low doping levels lies in the CuO_2 planes, and superconductivity also occurs in these planes.

A schematic phase diagram of cuprates is presented in Fig. 1-1. In the undoped region the antiferromagnetic (AFM) transition temperature (T_N) decreases with the doping level until it reaches zero at about 4% doping, where ordered antiferromagnetic state no longer exists. Above a certain doping level, superconductivity emerges. The superconducting transition temperature (T_C) increases with doping, up to a point of "optimal doping" (T_C^{max}). After this point further doping results in a T_C reduction. In the region between long range antiferromagnetic order and the region with no magnetic moments, there is a random arrangement of frozen moments. This phase, called spin glass, exist in these compounds also in the underdoped superconducting state.

As a result of the intimate relation between the superconducting state and the AFM, it is believed that superconductivity in the cuprates emerges from magnetic fluctuations in the same sense that BCS type superconductivity stems from lattice fluctuations (phonons). However, to date there is no clear evidence for correlation between the Néel temperature (namely, AFM interaction strength) and T_C , in the same sense in which BCS

superconductors with lighter nuclear mass result in superconductivity with higher T_C .

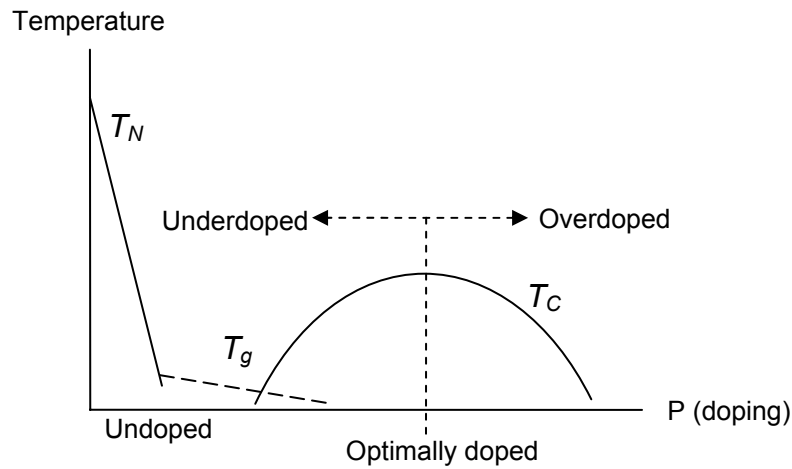


Figure 1-1: The main features of the cuprates phase diagram

In this work I will show, using a series of cuprates with minimal structural changes (symmetry, number of planes, and type of ions are unchanged), that T_C^{max} is an increasing function of T_N . In addition, I enhance our group's experimental demonstration of a simple relation between magnetic energy scale, doping, and T_C . These results leave very little doubt that cuprates' superconductivity is a result of magnetic fluctuations.

To fully understand my contribution, it is important to review two major experimental developments in cuprates' research that preceded this work (for more details see chapter 3). First, it was shown by Uemura [1] that all HTSC in the underdoped region satisfy the relation:

$$T_C \propto \frac{n_s}{m^*}, \quad (1.1)$$

where n_s is the superfluid density, and m^* is the effective mass.

Second, Kanigel et al. [2] provided experimental evidence that $1/m^*$ can be replaced by a magnetic energy scale, namely,

$$T_C = J_f \cdot n_s (\Delta p), \quad (1.2)$$

where J_f is the energy scale of the antiferromagnetic interaction (see section 3.2), which is now different for different families, Δp is doping measured from optimum, and n_s is a universal function of doping for all families.

The conclusions from this relation are that: (I) one should expect a correlation between T_C^{max} and the Néel temperature T_N of the parent antiferromagnetic compound, and, (II) there is a unique J_f for a given family.

The goal of this work is, as mentioned before, to demonstrate these two expectations. We confirm the first expectation by measuring the magnetic transition temperatures T_g and T_N using ZF μ SR on undoped CLBLCO samples. We demonstrate the second expectation by performing NQR measurements on YBCO samples with various oxygen concentrations. The NQR results show that in the YBCO system $T_C \propto n_s$, therefore J is constant for the YBCO family.

Chapter 2

Material – Structure and properties

2.1 YBCO

$\text{YBa}_2\text{Cu}_3\text{O}_y$ (YBCO) is a HTSC with 1:2:3 atomic ratio. As can be seen from the phase diagram in Fig. 2-1, at low temperatures it is tetragonal for $y < 6.4$ and orthorhombic in the superconducting state for $y > 6.4$.

The YBCO unit cell is shown in Fig. 2-2. In YBCO, apart from the CuO_2 planes, there are also one dimensional Cu-O chains. The copper in the chains is termed Cu(1) and the copper in the planes Cu(2). In YBCO_6 there are no Cu-O chains, and the compound is an antiferromagnetic insulator as shown by neutron scattering experiments [3]. The doping is achieved by inserting additional oxygen atoms, which form the Cu-O chains. At an oxygen content of 6.4, antiferromagnetic long range order disappears and the superconducting phase starts developing.

In a crystal form Y has a valence of +3, Ba of +2 and O of -2. The Cu(1) valence is +1 and therefore the Cu(2) valence changes from +2 to +3 with increasing oxygen doping. Hence, holes are formed in the plane. Cu^{+3} is non magnetic since its electronic spin is zero [4], while Cu^{+2} has a non vanishing electronic spin. For $y=7$ about 16% of the copper are Cu^{+3} . For $y=6$ all the copper ions are Cu^{+2} .

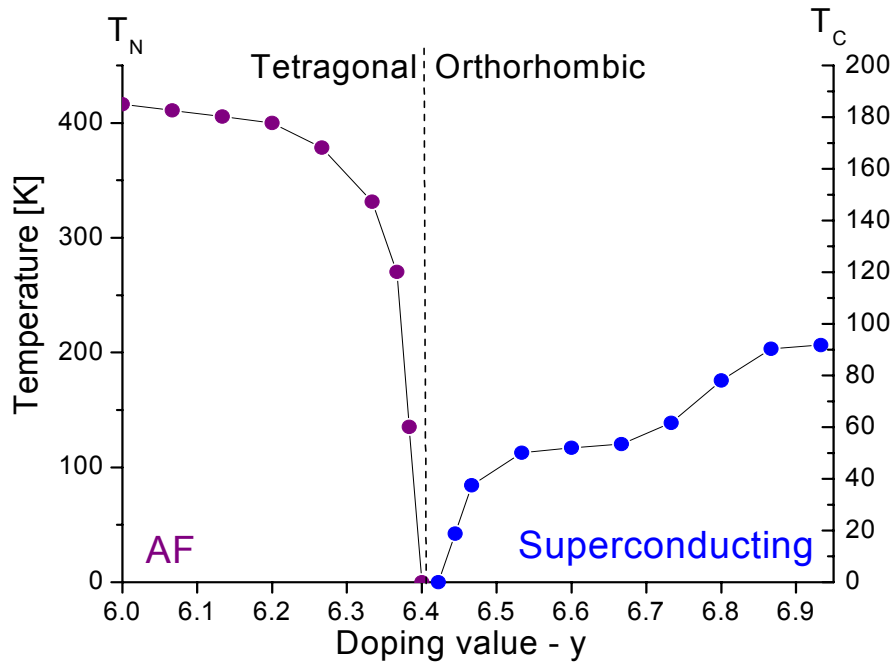


Figure 2-1: Phase diagram of YBCO

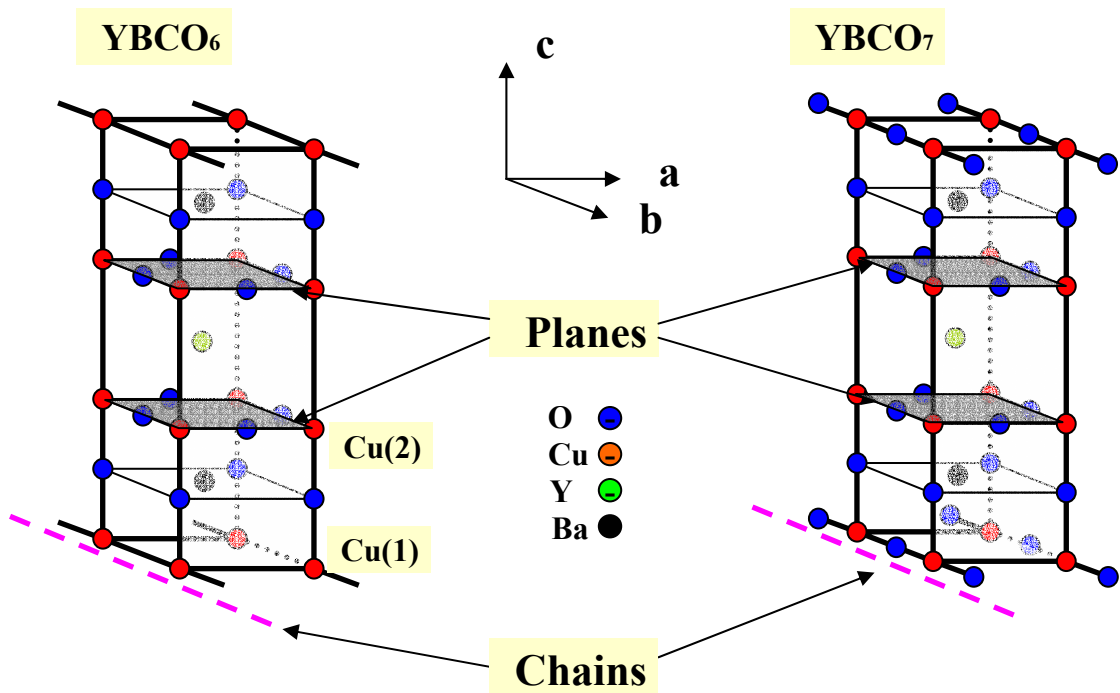


Figure 2-2: The YBCO unit cell

2.2 CLBLCO

$(\text{Ca}_x\text{La}_{1-x})(\text{Ba}_{1.75-x}\text{La}_{0.25+x})\text{Cu}_3\text{O}_y$ is a family of HTSC, which also belongs to the 1:2:3 systems. In comparison to YBCO, Ca occupies the Y site, and La occupies both the Y and the Ba sites. This compound is tetragonal in all its range of existence $0 \leq x \leq 0.5$ [5], so there are no ordered Cu-O chains like in YBCO. The oxygen atoms in the Cu(1) layer are distributed randomly with respect to the a and b directions.

The CLBLCO family is stable throughout all parabolic T_C curves, so one can synthesize samples ranging from the underdoped to the overdoped, by changing the O doping. By changing x, nearly parallel T_C vs. O doping curves are formed, as shown in Fig. 2-3. According to bond valence sum calculations [6], the hole concentration in the CuO_2 planes does not depend on x, but still the maximum value of T_C varies from $\sim 45\text{K}$ at $x=0$ to $\sim 80\text{K}$ at $x=0.4$.

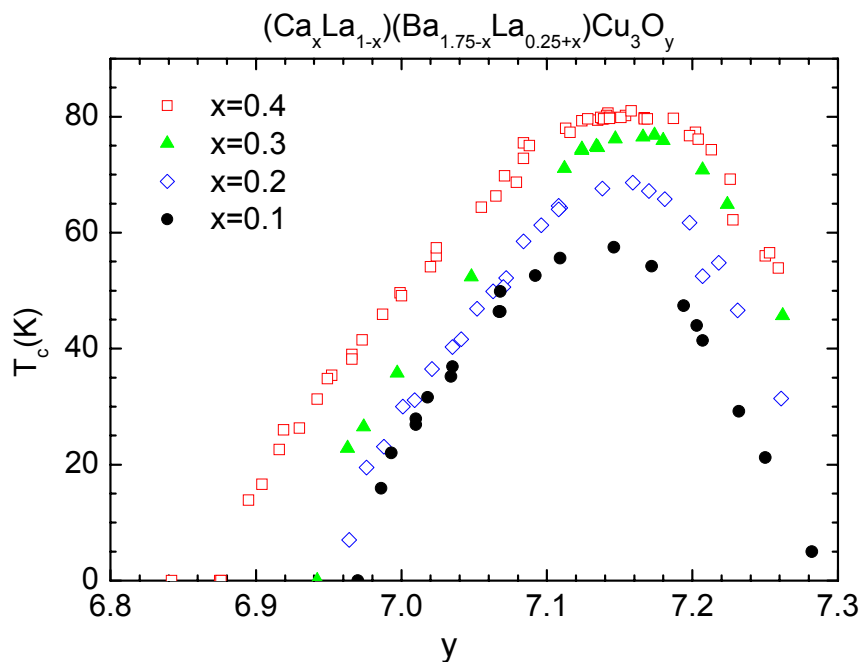


Figure 2-3: The variation of T_C with oxygen doping in CLBLCO for various values of x. taken from [7]

Chapter 3

Review of Previous Results

3.1 The Uemura relations

In the work originated by Uemura [1] and confirmed by many others including our group [8] a universal relation between the muon rotation line width σ (equivalent to relaxation rate) and T_C was found, namely,

$$T_C \propto \sigma. \quad (3.1)$$

The line width in turn is inversely proportional to the penetration depth squared [9] so that

$$\sigma \propto \lambda^{-2}. \quad (3.2)$$

Finally, according to the London theory [10]:

$$\lambda^{-2} \propto n_s / m^*. \quad (3.3)$$

Our group's measurements were performed on the [CLBLCO] $(\text{Ca}_x\text{La}_{1-x})(\text{Ba}_{1.75-x}\text{La}_{0.25+x})\text{Cu}_3\text{O}_y$ system (see chapter 2) in the entire doping region. They are presented in Fig. 3.1 together with results from other systems. Indeed the CLBLCO system satisfies the Uemura relation (Eq.1.1).

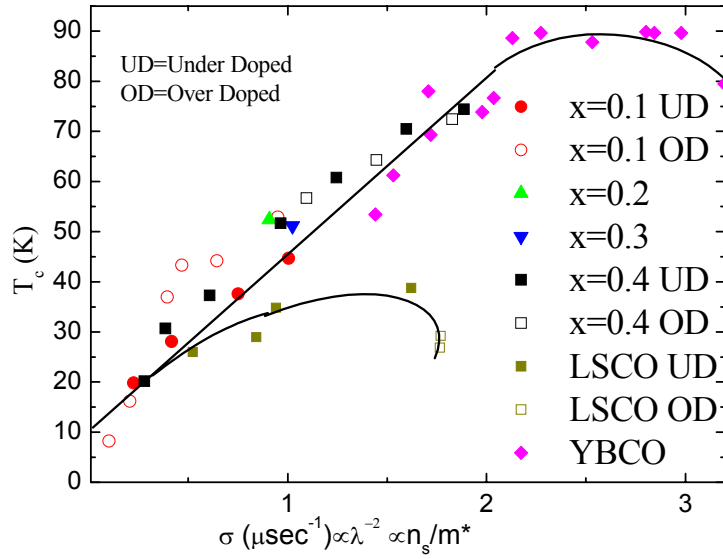


Figure 3.1: A Uemura plot showing T_C vs. the muon line width σ in a μ SR experiment for the CLBLCO, the LSCO and the YBCO families. σ is proportional to λ^{-2} which is proportional to n_s/m^* . λ is the magnetic penetration depth [2]

3.2 Scaling relation

The work of Kanigel et al [2] began with the $(\text{Ca}_x\text{La}_{1-x})(\text{Ba}_{1.75-x}\text{La}_{0.25+x})\text{Cu}_3\text{O}_y$ system, where every x represents a different superconducting family (see the phase diagram in Fig 2-3). The chemical doping measured from optimum, $\Delta y \equiv y - y_0$, was defined for each compound. y_0 is the doping level at which T_C is at maximum.

In order to make all superconducting domes converge into a single dome, Δy was multiplied by a different constant $K(x)$ for every family. The constant $K(x)$ represents the fact that not all the chemical holes (namely, not all the charge taken by the doping oxygen) turns into holes on the Cu-O plane and contributes to the superfluid density. On the plot of T_C/T_C^{max} vs. $\Delta p \equiv k(x)\Delta y$, all the curves merge into one. See Fig. 3-2A.

The same scaling, built to make the T_C domes coincide, was used on the T_g vs. y data (with no free parameters). The result is shown in Fig. 3-2B. All the lines of T_g/T_C^{max} vs. Δp merge into one line. This scaling method was then

applied to other compounds such as LSCO, YBCO and Bi-2212, for which T_g and T_C data exist in the literature and the result was the same.

To explain this scaling Kanigel et al. suggested to adopt the Uemura relation but modified the notation so that:

$$T_C = J_f \cdot n_s(\Delta p), \quad (3.4)$$

where J_f varies between different cuprates but does not depend on the oxygen doping. Thus the variation in T_C , for each family, originates in the variation in n_s - the superfluid density only. Hence we can write:

$$T_C^{\max} = J_f \cdot n_s(0). \quad (3.5)$$

Therefore we get

$$\frac{T_C}{T_C^{\max}} = \frac{n_s(\Delta p)}{n_s(0)}. \quad (3.6)$$

The family index has dropped out from this relation, hence all superconductors' curves merge into one function. Similarly, one expects the magnetic transition temperature to follow

$$T_g = J_f \cdot f(\Delta p), \quad (3.7)$$

where $f(\Delta p)$ is an unknown function of the doping.

Therefore the family index disappears again from the ratio

$$\frac{T_g}{T_C^{\max}} = \frac{f(n_s(\Delta p))}{n_s(0)} \quad (3.8)$$

and all curves merge into a single function. The coincidence of the curves suggests that the same energy scale J_f controls both the superconducting and the magnetic transition.

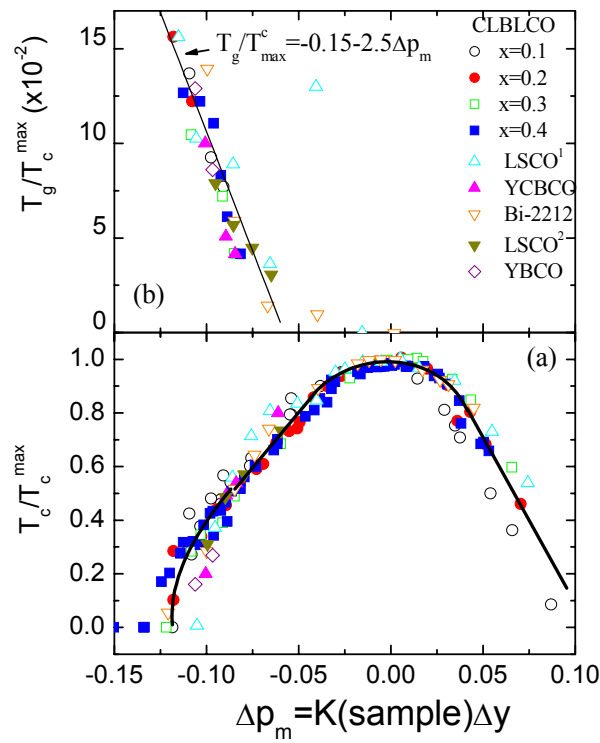


Figure 3-2: (a) T_c/T_c^{\max} and (b) T_g/T_c^{\max} as a function of $\Delta p = K_f \Delta y$ for several HTSC families. K_f is chosen so that T_c/T_c^{\max} vs. Δp of various cuprates families collapse into a single curve. As a consequence T_g/T_c^{\max} vs. Δp also collapse into a single line.

Chapter 4

EXPERIMENTAL METHODS

4.1 Nuclear Quadrupole Resonance (NQR)

The NQR technique can be applied for nonspherical nucleus only, such as the Cu nuclei with spin $I=3/2$. The energy of these nuclei inside a solid depends on their orientation. An example of that, for a nucleus that is elongated and is acted on by 4 charges, is shown in Fig. 4-1. When the nucleus' poles are close to the positive charges, the energy is higher than when the poles are close to the negative charges. The energy difference between one configuration to another is determined by the Electric Field Gradient (EFG), namely, the second derivative of the electrostatic potential $V(r)$ at the position of the Cu nuclei. The potential V depends on the surrounding charges.

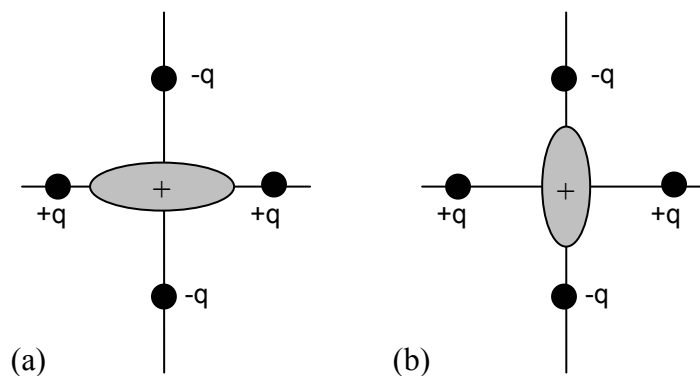


Figure 4-1: Different configurations of an oval shaped nucleus in a field of four charges. The configuration (b) is energetically favorable.

The NQR Hamiltonian is given by (see appendix A):

$$\hat{H}_Q = \frac{\hbar\nu_q}{6} \left[3\hat{I}_z^2 - \hat{I}^2 + \eta(\hat{I}_x^2 - \hat{I}_y^2) \right], \quad (4.1)$$

where ν_q is a frequency scale determined by the EFG components V_{zz} and η .

$$V_{zz} = \frac{\partial^2 V}{\partial z^2} \quad \text{and} \quad \eta \text{ is the asymmetry parameter } \eta = \frac{V_{xx} - V_{yy}}{V_{zz}}.$$

I_x, I_y, I_z are the operators of the total angular momentum of the nucleus.

For copper atoms in the CuO_2 planes of YBCO, z is the direction perpendicular to these planes.

The NQR measurement is done by applying 2 pulses of duration $t_{\pi/2}$ and $2t_{\pi/2}$ with a time interval τ between them, at Radio Frequency (RF) f (see section 4.1.1). The pulses are transmitted to a coil, which hold the sample inside it, and generate a field in the direction of the coil. This adds a time dependant perturbation term to the Hamiltonian:

$$H_{rf} = \omega_R \cdot \hat{n} \cos(\omega t) \quad (4.2)$$

where $\omega_R = {}^{63}\gamma B_1$ and ${}^{63}\gamma$ is the ${}^{63}\text{Cu}$ gyromagnetic ratio. $f = \omega/2\pi$ is the transmission frequency.

The resonance condition is met when the frequency f matches the energy difference between the two states created by the quadrupole interaction described in the Hamiltonian of Eq (4.1). When this resonance condition is met an echo is formed in the coil.

For a spin 3/2 nuclei like Cu, the 2 energy levels in the NQR Hamiltonian are two doublets, so there is one resonance frequency, and it can be shown to be (see appendix A and Ref.[11]):

$$f_{NQR} = \hbar\nu_q \sqrt{1 + \frac{\eta^2}{3}}. \quad (4.3)$$

4.1.1 FID (Free Induction Decay) and Spin echo

A NQR experiment on a nuclear spin $3/2$ is very similar to a NMR experiment on a nuclear spin $1/2$. For simplicity we will explain the FID and spin echo sequence using the example of NMR spin $1/2$.

In NMR one applies a magnetic field in the z direction so the nuclei spins are in the z direction (the z direction in our NQR experiment is defined by the EFG and is perpendicular to the Cu-O planes). After applying a RF pulse with length $t_{\pi/2}$ in the x direction, the spin rotates from the z direction to the x - y plane ($\pi/2$ pulse). After the pulse ends the spins start to rotate in the x - y plane and the magnitude of the vector decays with time. This induces a voltage in the coil, which can be measured. This pulse is called FID (free induction decay).

The problem with the FID sequence is that the signal appears immediately after the pulse. That is why we used the spin echo sequence. In this sequence a $\pi/2$ pulse is first applied, this pulse rotates the magnetization down into the x - y plane, the spins are now rotating in this plane and begin to dephase. After a time τ a second pulse with length $2t_{\pi/2}$ is applied. This pulse rotates the magnetization by 180° about the x axis back to the x - y plane. The π pulse causes the magnetization to at least partially rephase and to produce a signal called an echo after a time τ from the second pulse. A schematic description of a spin echo sequence in NMR is shown in Fig. 4-2.

In NQR on spin $3/2$ the situation is slightly more complicated. For spin $3/2$ nuclei there are two energy levels in the NQR Hamiltonian as explained in appendix A. One level is for spin $+1/2$ and the other is for spin $+3/2$. So in the NQR case there is no net polarization in the z direction. After the $\pi/2$ pulse all the spins are in the x - y plane and there is still no polarization. But now, the rotation in the x - y plane is opposite for the "up" and "down" spins, and after some time polarization is obtained in the x - y plane, and then the dephasing starts.

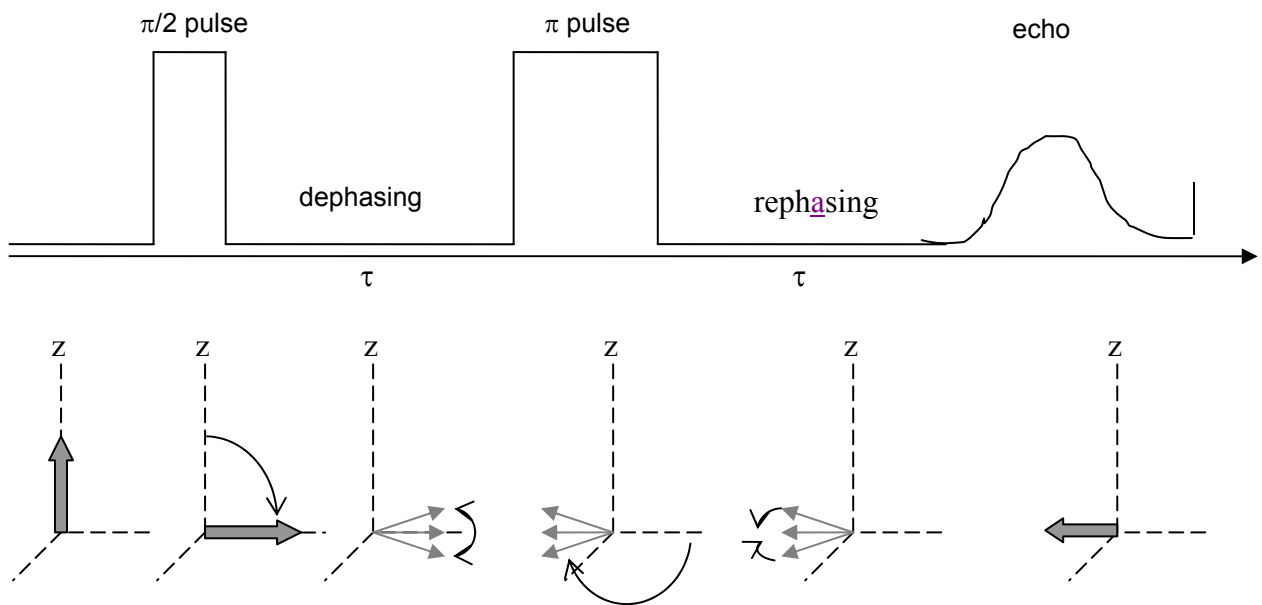


Figure 4-2: A schematic description of a spin echo sequence. The two pulses are followed by a Gaussian shaped echo. The schematic polarization graphs are for spins $1/2$ in NMR

4.1.2 The experimental conditions

In this work we measured the echo intensity of YBCO while sweeping the transmission frequency f . Changes in the resonance frequency of the Cu nuclei suggests changes in the EFG, and in the surrounding charges and distances.

The NQR data was obtained by applying a spin echo sequence with $t_{\pi/2}$ of $1.2\mu\text{sec}$ and τ of about $24\text{-}30\mu\text{sec}$. The actual spectral points were obtained by signal averaging of between 200,000 to 300,000 scans with a delay time between scans of 3msec.

The measurements were performed in a coil tunable from 20 to 33 MHz, at a temperature of 100K. This temperature is above T_C for all samples. NQR experiment at temperature below T_C is more difficult since the superconductor rejects the external magnetic field.

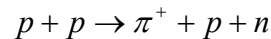
4.2 Muon Spin Relaxation (μ SR)

μ SR is a technique that allows the study of magnetic properties of materials in a microscopic level. This technique uses the muon, a short lived particle, whose spin and charge are very sensitive local magnetic probe of matter. The muon is injected into the matter, its spin then rotates around the local magnetic field, and then it decays to a positron in the direction of the muon spin. The decayed positron direction in time indicates the muon's spin time evolution.

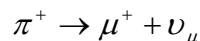
The μ SR experiments in this work were performed at ISIS pulsed muon facility at Rutherford Appleton Laboratory in the UK. The samples were measured in a ^4He cryostat, a CCR or a furnace, depending on the transition temperature. The μ SR samples were all sintered pellets. All the measurements were performed in zero field.

4.2.1 Muon production, implantation and decay

Experiments in condensed matter require high intensities and flux, this is achieved by using high energy proton beams, produced in cyclotrons. The protons collide with nuclei in an intermediate target and produce pions via:



the pions then decay into muons:

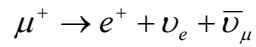


Where ν_μ is the muon-neutrino.

Most positive muon beams at a μ SR facility are generated from pions decaying at rest in the target surface. These muons, known as surface muons, have zero momentum. So, in order to conserve momentum, the muon and the neutrino have opposite spin. The neutrino always has negative helicity (its spin is antiparallel to its momentum), and thus the muon spin has to be similarly aligned. In this way a muon beam that is 100% spin polarized can be produced.

The muons hit the target with energy of 4MeV, and lose their energy very quickly (in 0.1-1nsec) by various scattering processes, all of Coulombic origin, so there is no influence on the muon's spin. After stopped, the muons precess

according to the local magnetic field and decay after a time t with probability $\exp(-t/\tau)$. $\tau = 2.2\mu\text{s}$ is the lifetime of the muon. The muon decays in a three body process:



The decay involves the weak interaction and violates parity. This leads to the positron being emitted preferentially along the direction of the muon's spin at the time of the decay. The angular distribution of the emitted positrons is shown in Fig 4-3. This way the polarization of an ensemble of muons can be followed, by detecting the emitted positrons. The positrons are detected using an array of plastic scintillators, connected via a light-guide to a set of photo-multipliers.

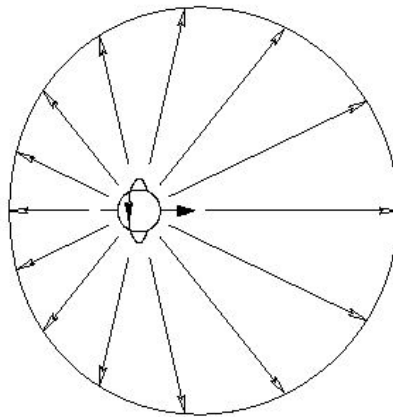


Figure 4-3: The angular distribution of emitted positrons with respect to the initial muon-spin direction.

4.2.2 Experimental setup

Muon experiments can be performed in two different ways depending on the time structure of the muon beam. In a Continuous Wave (CW) facility, like in the Paul Scherrer Institute (PSI) in Switzerland, the muons arrive at the sample without any distinct time structure. When the muon enters the experiment it is detected and starts a clock. When the positron is detected in one of the detectors, the clock is stopped. The advantage of this type of muon beam is that the time resolution is quite small, and so fast relaxing signals can be detected. On the other hand, if a second muon arrives before the first one

has decayed then there is no way of knowing whether the emitted positron came from the first or second muon, so this event must be disregarded. This limits the maximal time for which the polarization of the muons can be traced to about $10\mu\text{sec}$.

In pulsed beam facilities, like ISIS at the Rutherford Appelton Laboratory in the UK, a large number of muons arrive in a very intense pulse so there is no need to detect when each muon arrives. The detection of the positrons is then made and each event is timed with respect to the arrival of the pulse. In this method the entire incoming muon intensity can be used and there is almost no background in the μSR signal. This allows detection of muon decay events beyond 10 muon lifetimes, meaning $\sim 20\mu\text{sec}$. The drawback of this method is that the width of the muon pulse limits the time resolution, because all the muons in a given pulse are counted together, and the muons do not all arrive simultaneously.

Most of the samples in this work were measured in the pulsed beam source in ISIS, because the ability to detect the polarization up to times of $20\mu\text{sec}$ and the absence of background signal makes it more suitable for our zero field experiments.

Once implanted in the sample, the muon spin precesses in the presence of the local magnetic field B with angular frequency $\omega_{\mu} = \gamma_{\mu}B$ where γ_{μ} is the gyromagnetic ratio for the muon. This is known as Larmor precession.

Unlike other resonance techniques, like NMR or ESR, no electromagnetic field is necessary, since the muon beam is initially polarized, and the precessing muon can be followed directly from the emitted positron.

A schematic diagram of the experiment is shown in Fig 4-4. A muon, with its polarization aligned antiparallel to its momentum, is implanted in a sample. If it decays immediately, then it will not have time to precess and a positron will be emitted preferentially into the backward detector. If it lives a little longer it will have time to precess so that if it lives for half a revolution the resultant positron will be preferentially emitted into the forward detector.

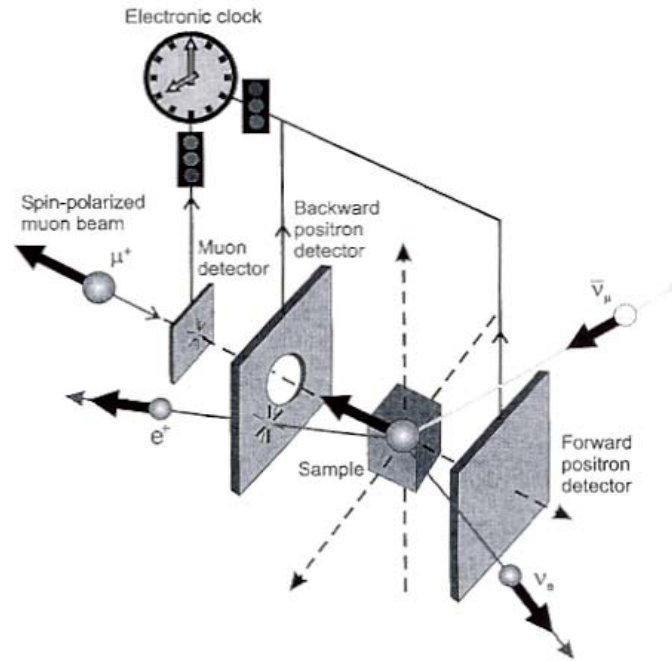


Figure 4-4: Schematic illustration of a μ SR experiment.

Fig 4-5 shows the time evolution of the number of positrons detected in the forward and backward detectors. Because the muon decay is a radioactive process these two terms sum to an exponential decay, with a decay constant that is the lifetime of the muon. Hence the time evolution of the muon polarization can be extracted from the normalized difference between the number of positrons detected at the forward and backward detectors,

$$A(t) = \frac{N_B(t) - N_F(t)}{N_B(t) + N_F(t)}. \quad (4.4)$$

$A(t)$ is called the asymmetry plot. The maximum value of the asymmetry plot depends on the initial beam polarization, the intrinsic asymmetry of the weak decay, and the exact structure of the detectors system. It is usually around 0.25.

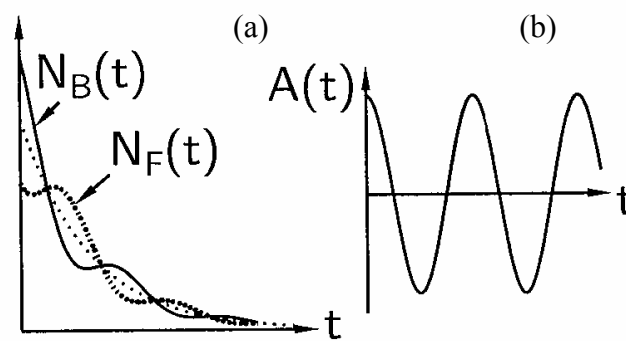


Figure 4-5: (a) The number of positrons detected in the forward and backward detectors. (b) The Asymmetry function. Taken from [12]

μ SR can be performed with no applied external field (ZF), as was done in this work, or with either transverse (TF) or longitudinal (LF) fields applied with respect to the initial muon spin direction. In the ZF case the muons will precess according to the internal field in the sample under study and reveal the internal field distribution. This method is very sensitive to detecting weak internal magnetism. In the TF case the muon will precess about the applied field, with frequency proportional to the size of the field at the muon site in the material. Any dephasing in the observed oscillation indicates either an inhomogeneous internal field distribution or spin-spin (T_2) relaxation. In LF there is no spin precession, but spin relaxation, due to inhomogeneous field distributions or spin-lattice (T_1) relaxation processes.

4.2.3 Muons in matter in Zero Field

Muons in magnetically ordered materials precess in the internal magnetic field and result in signals proportional to that magnetic field. The very large magnetic moment of the muon makes it very sensitive to extremely small magnetic fields (~ 0.1 G), and so it is useful in the study of materials where the magnetic order is random or very short range.

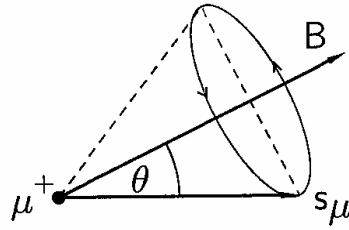


Figure 4-6: Muon spin precession about the magnetic field at an angle θ

Fig. 4-6 shows the muon-spin precession in a magnetic field. If the local magnetic field at a muon site is at an angle θ to the initial muon spin direction, when the muon is implanted, the muon spin will precess around a cone of angle θ about the magnetic field. The polarization in the z direction (and the positron asymmetry) will be:

$$G(t) = \cos^2 \theta + \sin^2 \theta \cos(\gamma_{\mu} B t). \quad (4.5)$$

If the direction of the local magnetic field is random then averaging over all directions gives:

$$G(t) = \frac{1}{3} + \frac{2}{3} \cos(\gamma_{\mu} B t). \quad (4.6)$$

If the strength of the local magnetic field has a Gaussian distribution with width Δ/γ_{μ} centered on zero, then averaging over this field distribution gives:

$$G(t) = \frac{1}{3} + \frac{2}{3} e^{-\Delta^2 t^2 / 2} (1 - \Delta^2 t^2). \quad (4.7)$$

This polarization is known as the Kubo-Toyabe polarization, shown in Fig. 4-7. This relaxation function is observed experimentally in cases where the origin of the internal field is frozen random nuclear magnetic moments.

If the form of the internal field distribution was different then this would affect the form of the relaxation line.

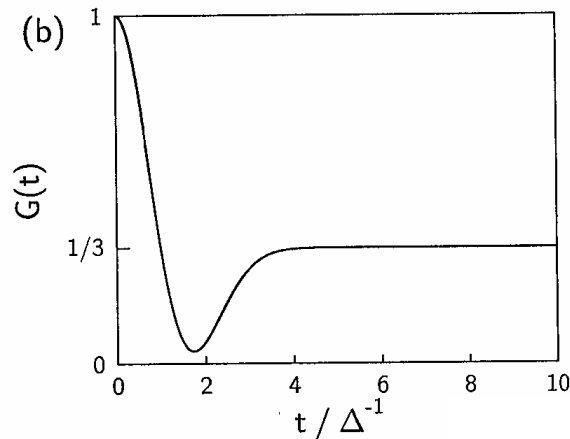


Figure 4-7: The Kubo-Toyabe polarization, the relaxation of the muon-spin due to a Gaussian field distribution.

In general when there is an anisotropic distribution of fields the average over the polarization in Eq. (4.5) is

$$G(t) = \frac{1}{3} + \frac{2}{3} \int_0^{\infty} \rho(|B|) \cos(\gamma|B|t) B^2 dB \quad (3.8)$$

where $\rho(|B|)$ is the distribution of $|B|$.

Magnetic and non magnetic regions co-existing in the same specimen result in distinct signals whose amplitudes are proportional to the volume of the sample occupied by the particular phase.

4.3 Sample preparation

Both the YBCO and the CLBLCO samples are prepared by solid state reaction. Raw powders are machine milled and baked in air at 950°C for one day and re-grounded repeatedly 3 times. Then the powder is pressed into pellets, and the pellets are sintered for 70h in flowing oxygen at 960°C, and cooled at a rate of 10°/h.

Different oxygen content in the YBCO samples is achieved by oxygen reduction in a tube furnace in flowing oxygen at the right temperature. The reduction temperature determines the oxygen doping level in the material. After 24h in the furnace the samples are quenched in liquid N₂. The samples with very low doping (under y=6.6) are quenched in liquid Ar. The reason for that is that the liquid N₂ is not pure and contains O₂ molecules. At low doping

levels there is a greater chance that these molecules would penetrate the sample during the quenching. This causes the samples to become oxygen inhomogeneous and the transition to superconductivity wider. [13].

In CLBLCO samples at high doping levels the reduction is done in the same way as in the YBCO samples. Under a certain doping level (about $y=6.7$), the reduction is made with flowing nitrogen instead of oxygen (so that more oxygen can come out of the sample at a certain furnace temperature) and quenched to room temperature.

The oxygen content is measured by iodometric titration; this method is capable of measuring y with an error of ± 0.001 .

4.3.1 Orientation

For better signal intensities in the NQR measurements, all the YBCO powder samples were oriented. About 1gr of powder, mixed with StayCast glue, was inserted into a Teflon cylinder of length 1.2cm and 0.5cm diameter. The sample was then inserted into a magnetic field of 8.0033T, and shaken for 30 minutes at room temperature. The shaking was done by connecting it to an electromagnetic relay with a voltage of 10V and 25Hz square wave.

The orientation process aligns the YBCO grains so that all the (00l) planes are perpendicular to the magnetic field. This is because the susceptibility of each grain in the powder, which is a single crystal, creates the maximum magnetic moment in the direction of the crystal c axis. So after the orientation we identify the z direction of the YBCO crystal with the magnetic field direction. The orientation was done so that the Z direction was perpendicular to the NQR coil direction.

4.3.2 Enriched samples

Previous Cu NQR measurements on YBCO [see Ref. 14,15,16,17] were performed on samples containing both Cu isotopes, Cu^{63} and Cu^{65} , so the results consisted of doublets of Cu^{63} - Cu^{65} .

In this work for a more clear understanding of the NQR signals, the YBCO samples were all made of enriched copper, meaning that these samples contained only the Cu^{63} isotope.

Chapter 5

RESULTS

5.1 NQR on YBCO

We measured YBCO_y samples with the oxygen stoichiometry varying from $y=6.4$ to $y=7$. We performed frequency sweep measurements of the NQR echo intensity. The measured signal intensities were divided by the square of the frequency and plotted vs. the frequency. The results are shown in Fig. 5-1.

The intensity results in each graph are normalized to the maximum intensity for that sample and are plotted in arbitrary units. The echo intensity depends on a number of factors (such as: the material quantity, the time τ between the sequence pulses, the matching and tuning of the circuit impedance). These factors differed from sample to sample, that is why we do not compare the peaks intensity between samples, only the peaks location in the frequency axis.

Previous work [14,15] showed that at high doping levels ($Y>6.5$) only Cu(2) signals are present in the frequency range presented in Fig. 5-1. As doping is lowered a signal from Cu(1) with empty chains appears around 30MHz. It is also known from previous work [16] that for $Y=7$ at 300k the resonance frequency for Cu(2) is at 31.2MHz. Indeed we see in Fig. 5-1 that for $Y=7$ there is only one line around 31.4MHz.

Fig. 5-1 shows that as the doping is lowered two more lines appear. This is due to the different ionic environments around the Cu(2) nuclei (Fig 5-4). The solid lines in Fig. 5-1 are fits to Gaussians, performed in order to determine the resonance frequencies, and to compare the intensity ratio between the lines peaks for each sample (Fig. 5-3).

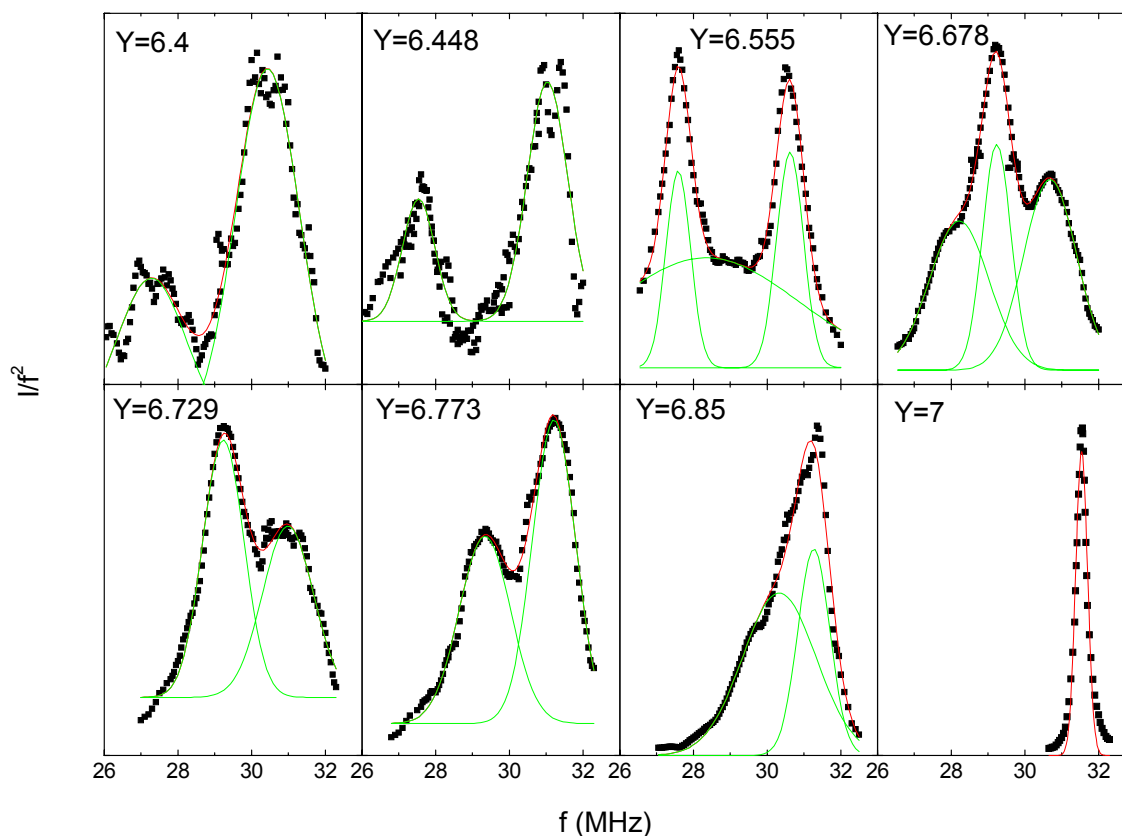


Figure 5-1: NQR frequency sweep on YBCO. The dotted line is the experimental result. The solid line is a Gaussian fit performed in order to determine the resonance frequencies.

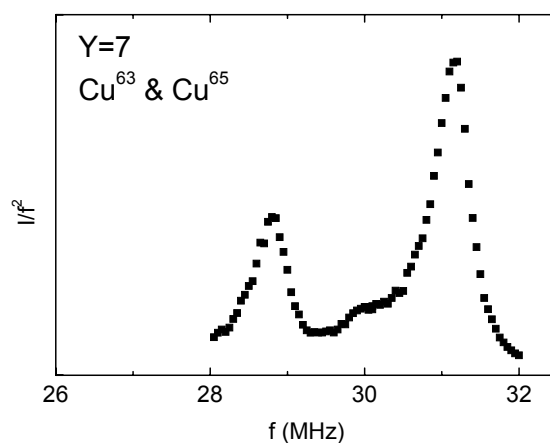


Figure 5-2: NQR frequency sweep for YBCO₇ with both isotopes of copper. Instead of one resonance peak there is a Cu⁶³ - Cu⁶⁵ doublet.

Fig 5-2 shows an example of a frequency sweep performed on an YBCO_7 sample that contains both isotopes of copper. Instead of one resonance peak, when there is only the Cu^{63} isotope, there is a Cu^{63} - Cu^{65} doublet. This helps to demonstrate the advantage of the enrichment. At lower doping, without the enrichment, each resonance frequency would be a doublet and it would be impossible to distinguish between the different resonance frequencies.

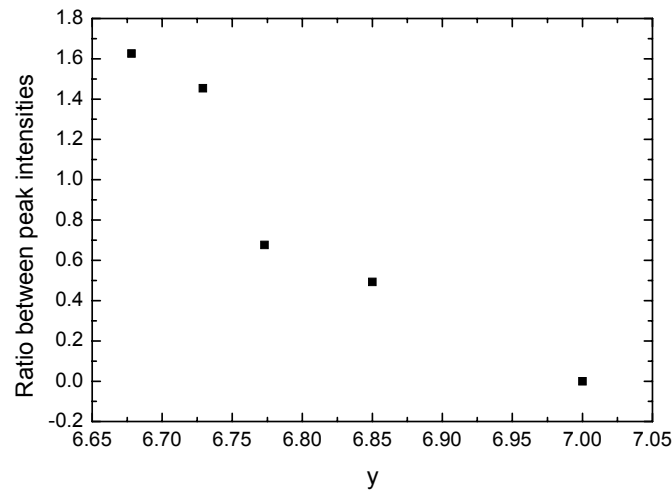


Figure 5-3: The intensity ratio between the 29MHz line and the 31MHz line as a function of the doping. As the doping decreases and oxygen is being removed from the chains the line of a $\text{Cu}(2)$ with chain half full (29MHz) increases on the expense of $\text{Cu}(2)$ with the chains full.

As the doping decreases, the $\text{Cu}(2)$ environment changes for a number of reasons:

- Oxygen is being removed from the chains so the ionic environment changes. The $\text{Cu}(1)$ can have oxygen coordination of 2, 3 or 4 (see Fig. 5-5)
- The lattice constants change. For example the bridging oxygen in the Ba-O plane moves away from the $\text{Cu}(2)$ towards the $\text{Cu}(1)$. This can change the orbital energies at the $\text{Cu}(2)$ site [14].
- Removal of oxygen from the chains has a direct effect on the electronic structure of the $\text{Cu}(2)$ sites. The number of holes in the Cu-O plane changes.

The NQR peaks for all the YBCO samples are summarized in Fig. 5-4. This graph shows the frequencies of the NQR peaks as a function of the oxygen doping y . The graph shows three different peaks. Each peak moves to lower frequency as the oxygen doping decrease.

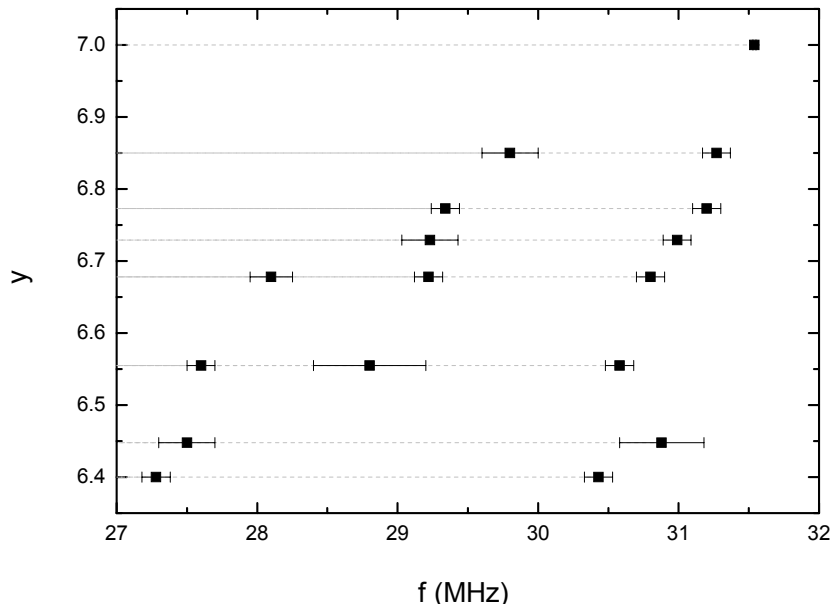


Figure 5-4: The oxygen doping level in YBCO as a function of the NQR frequencies

We believe that the three different peaks are a result of three different ionic environments (Fig 5-5). The first peak around 31MHz belongs to Cu(2) with the chains full, like in YBCO₇. (At low doping this peak is gradually replaced by the Cu(1) peak with empty chains). The second peak, around 29MHz, is a Cu(2) with chain half full, meaning the Cu(1) has a coordination of 3. The last peak, around 27.5MHz is a conducting Cu(2) site with empty chains next to it. This last assumption is based on the experiment done by Vega [14]. In this experiment the NQR data was taken with different delay time between scans so that both short (~1msec) and long (~500msec) T_1 signals were measured. The short T_1 signals indicated a rapid relaxation rate due to metal-like conducting electron dynamics. From that he concluded that the short T_1 signal around 27MHz is a conducting Cu(2) associated with a

conducting two-coordinated Cu(1). This peak is not found in YBCO_6 . In this compound the Cu(2) signal is not observed in this frequency range due to the antiferromagnetic ordering of the electron spin in the plane, that shifts the signal beyond the detection range.

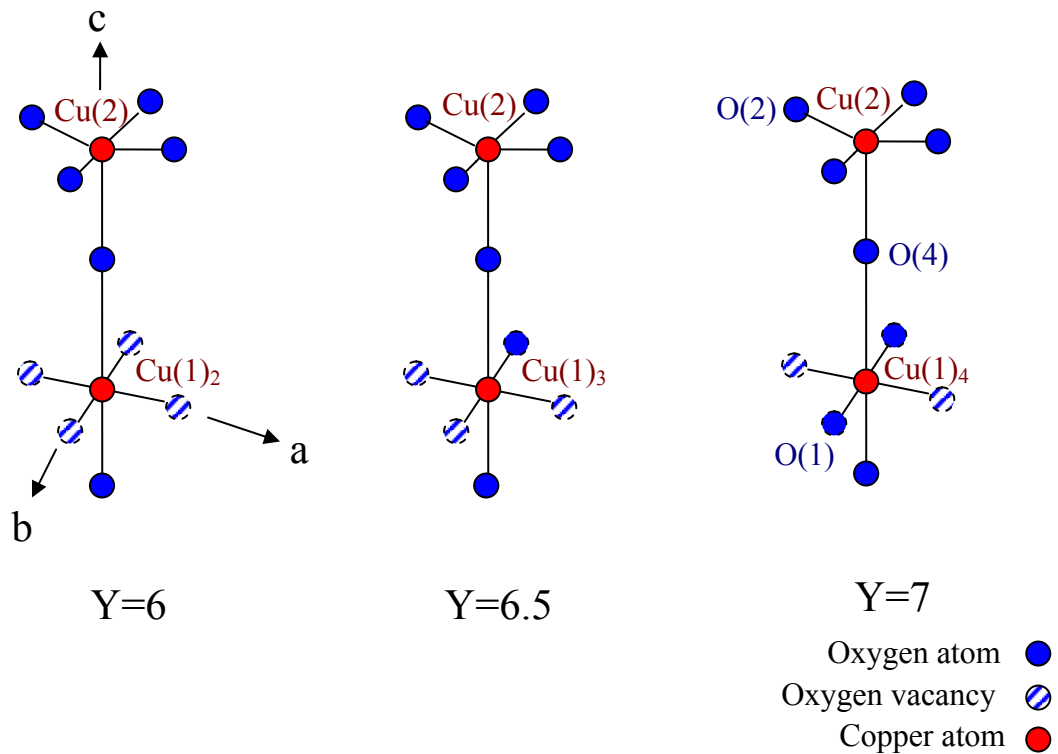


Figure 5-5: Schematic illustration of the Cu site with locally different oxygen coordinations.

5.2 μ SR on CLBLCO

We measured three families of $(\text{Ca}_x\text{La}_{1-x})(\text{Ba}_{1.75-x}\text{La}_{0.25+x})\text{Cu}_3\text{O}_y$ with $x=0.1, 0.3$ and 0.4 . The oxygen doping ranged from $y=6.4$ to the point where superconductivity appears. Four typical muon asymmetry plots are shown in Fig. 5-6 for four different samples.

In order to determine the magnetic transition temperatures T_g and T_N , we fit the data to a sum of two functions. The first function is the Kubo-Toyabe function shown in Fig. 4-7. This part describes the polarization resulting from frozen random nuclear magnetic moments. The second function is a rapidly relaxing function that describes the relaxation in the magnetic areas. In these areas there are electronic moments that freeze in a random orientation [2].

So the fit to the data is:

$$A_z = A_n \exp\left(\frac{-\Delta^2 t^2}{2}\right) + A_m \exp(-\sqrt{\lambda}t). \quad (5.1)$$

A_n is the amplitude of the nuclear part, A_m is the amplitude of the magnetic part and λ is the relaxation rate of the magnetic part. Above the transition, only the frozen nuclear moments are present and A_m is close to zero. As the temperature decreases, the electronic magnetic part increases and so does A_m , at the expense of A_n .

Δ , the relaxation rate of the nuclear part was determined at high temperatures and then kept constant throughout the temperature change. The sum $A_m + A_n$ is also constant throughout the temperatures and is equal to the initial asymmetry at high temperatures.

The solid lines in Fig. 5-6 are the fits to the data using Eq. 5.1. At low T a third, oscillating component, is added to the fit. However, its properties will not be discussed here since we are interested only in T_N .

We determined the transition temperature as the temperature at which A_m is one half of the total muon polarization. An example of that is shown in Fig. 5-7. This Figure shows the asymmetry plots of two samples, with $x=0.1$ and $x=0.4$, both with the same oxygen doping of 6.61 and two more samples with oxygen doping of 6.425. At oxygen doping of 6.61 the $x=0.1$ has a higher T_N , but at oxygen doping of 6.425 the sample with $x=0.4$ has a higher T_N .

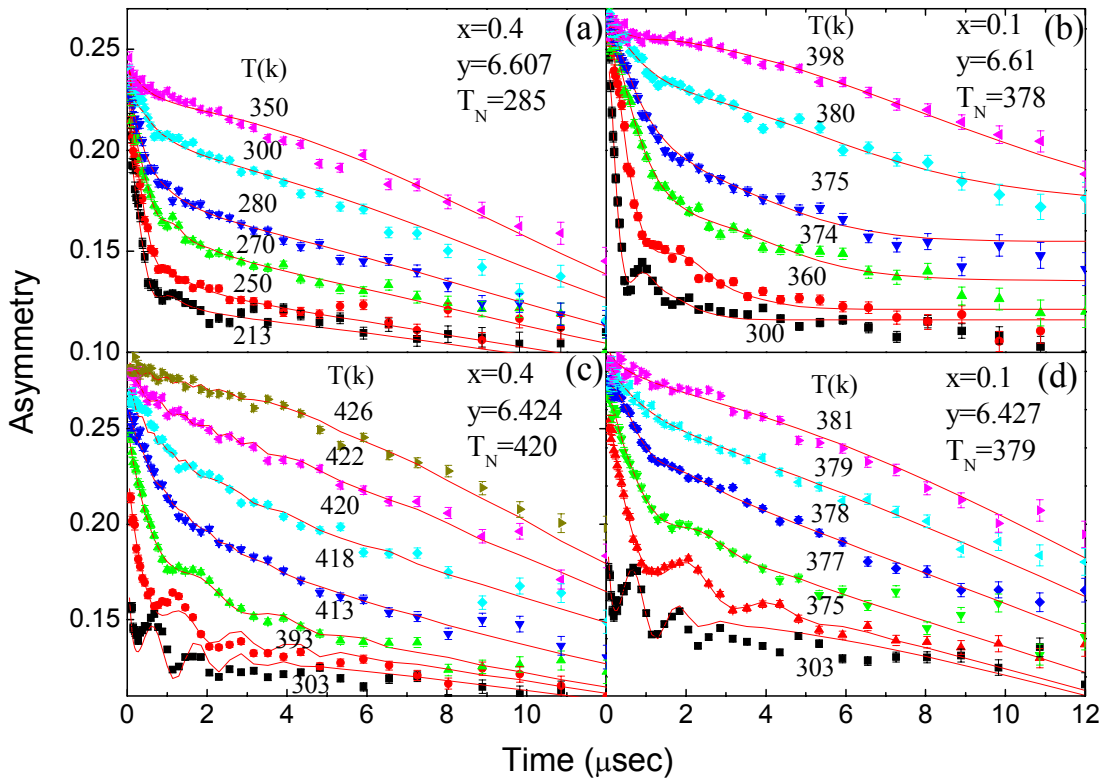


Figure 5-6: Asymmetry plots for varies temperatures for four CLBLCO samples

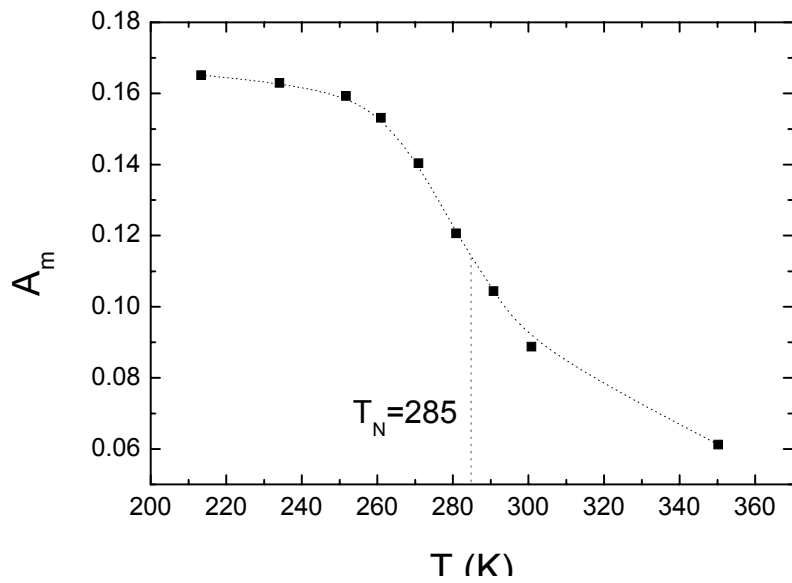


Figure 5-7: The magnetic amplitude A_m as a function of temperature for a sample with $x=0.4$ and $y=6.607$

Chapter 6

DISCUSSION

6.1 NQR on YBCO

Fig. 6-1 shows the location of the NQR resonance frequencies as a function of T_C . The solid lines are fits of the data to three lines with the same slope. The fit was done so that in the first line, around 31.5MHz, the last two points at low doping were not included, since in low doping at this frequencies there is also a signal from the Cu(1). This fit captures the data quite well.

To interpret this result we follow Haase et al. [18]. They could not distinguish between the different environments and focused only on high doping levels. Based on the data available to them, and their assumption that $\eta=0$, they suggested three main contributions to the EFG of the Cu(2) nucleus:

- i. The 3d hole concentration on the copper ion.
- ii. There is a virtual hopping of electrons from neighboring oxygen ions to unoccupied 4d orbitals of Cu.
- iii. The electric field of distant ions.

Therefore the NQR frequency is proportional to:

$$f \propto A \cdot n_d - B \cdot \beta^2 (8 - 4n_p) + C. \quad (6.1)$$

where n_d is the number of Cu holes (with $d(x^2-y^2)$ symmetry). Since n_p is the number of oxygen holes, $(8-4n_p)$ is the number of electrons in the neighboring oxygen and β^2 is the probability to jump to the Cu 4d orbital. Finally, C is related to the contribution of distant ions.

Based on the data available to Haase et al. they claim that for $y > 6.6$ ($T_C > 60$), doping increases the hole content only on the oxygen in the plane and not on the copper. This means that at these doping levels n_d is a constant.

So according to Eq. 6.1, in the doping region from $y=6.6$ to $y=7$, the NQR frequency is proportional to the number of holes in the CuO_2 plane.

Our ability to fit all three environments with a single slope means that in fact doping increases the hole content only for the oxygen at least from $y=6.4$ ($T_C=28\text{K}$).

The difference in the NQR frequency of the three different environments could be associated with different C values in Eq. 6.1.

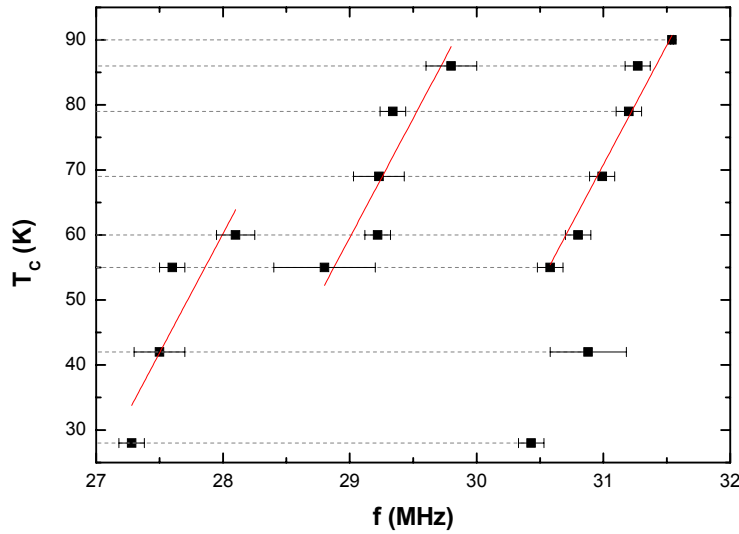


Figure 6-1: T_C for different YBCO samples as a function of the NQR frequencies. The solid lines are fits of the data to three lines with shared slope ($dT_C/df=37\pm 4$ (K/MHz)).

Hence, according to Haase, and assuming that all the free charge is part of the superfluid density [19] (so that $n_s = \Delta n_p / 2$), we find that:

$$\Delta f = \alpha \cdot n_s. \quad (6.2)$$

Haase predicts that $\alpha \cong 45 \text{ MHz}$

From the results in Fig. 6-1 we observed that the change in the NQR resonance frequency of the copper in the planes is proportional to T_C , for each type of ionic environments:

$$\Delta T_C = T_C = 37 (\text{K} / \text{MHz}) \cdot \Delta f. \quad (6.3)$$

Therefore, from Eq. 6.2 and 6.3 we can write the relation demonstrated in chapter 3:

$$T_C = J_f \cdot n_S \quad (6.4)$$

provided that $J_f = 37 \cdot \alpha(K)$.

Using YBCO's $T_C=90K$ and $n_S=0.08$ we find $J_f = 90/0.08(K) = 1125(K)$ or:
 $\alpha = 30.4MHz$.

This is 50% different from Haase's calculated α . Nevertheless, T_C is proportional to n_S so we conclude that for the YBCO family J_f is a constant and is independent of the oxygen doping.

In the Uemura relation in Eq. 1.1, T_C is proportional to n_S/m^* . The NQR results allowed, for the first time, to distinguish between n_S and m^* and indicated that m^* is independent of doping.

6.2 μ SR on CLBLCO

The results of the magnetic transition temperatures T_g and T_N are presented in Fig. 6-2 along with the superconducting transition temperature T_C . The T_g data in the superconducting region are taken from [2].

In the T_C data shown in Fig. 6-2, the family with a higher Ca concentration (higher value of x), has a higher value of T_C^{max} . This suggests a higher J_f according to Eq. 3.5 (provided that the superfluid density at the optimally doping is the same for all families). This suggests that T_N should also increase as the Ca content increases, at the heavily underdoped region.

In Fig. 6-2 T_g , the magnetic transition temperature to a spin-glass-like state is higher for lower Ca concentrations. As the oxygen doping decreases and the samples become long ranged antiferromagnets, the magnetic transition temperature increases, long range order is established, and we rename the critical temperature T_N . Up to a doping of about $y=6.5$, the $x=0.1$ samples still have a higher T_N . The point $y\sim 6.5$ is a crossing point, and at lower doping the family with higher x has the higher T_N .

At very low doping it seems like T_N saturates. $x=0.1$ has a T_N of about 380k and $x=0.4$ has a T_N of about 420k. With extrapolation we can conclude that for no oxygen doping CLBLCO samples with higher Ca concentration have a higher T_N , and therefore a stronger antiferromagnetic interaction and a higher value of J . The relation between T_C^{max} and T_N is presented in Fig. 6-3. This is the first plot of a correlation between T_N and T_C^{max} in a system with nearly no structural changes.

Therefore, at the higher doping levels the family with a higher T_C^{max} has a lower magnetic transition temperature, due to the unknown dependence of the doping (See Eq. 3.7). However this work showed that at very low doping, where T_N is determined primarily by the coupling constant J , the family with higher T_C^{max} also has a higher magnetic transition temperature.

However, it should be emphasized that when attempting to continue the scaling relation discussed in chapter 3, we discovered that this relation no longer holds in the non superconducting samples. Therefore, at present the common energy scale for superconductivity and magnetism is only correct locally within the superconducting dome.

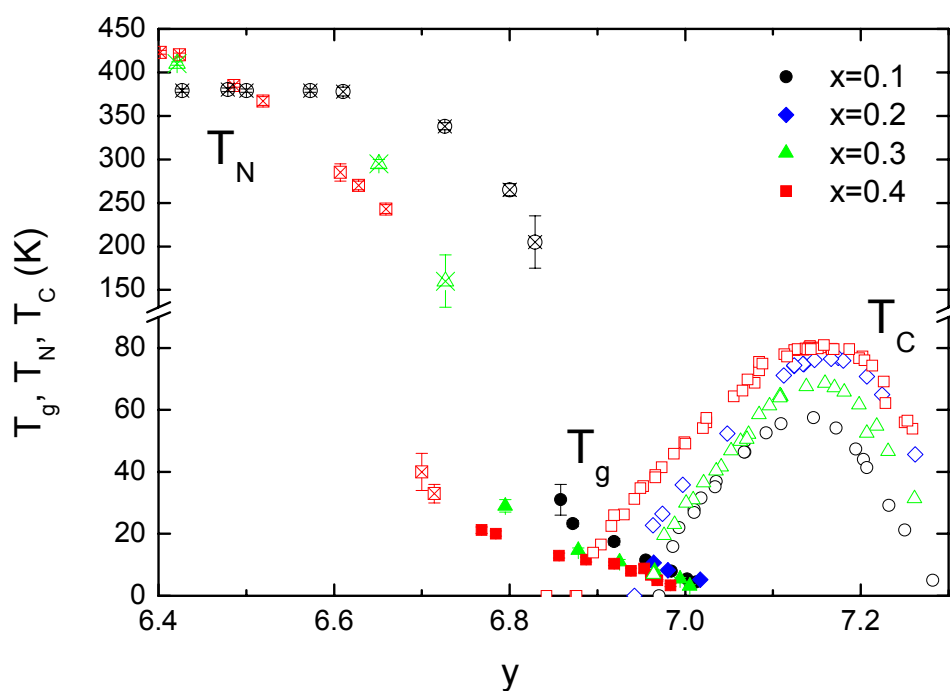


Figure 6-2: T_C , T_g , and T_N as a function of the oxygen doping for four families of CLBLCO. The empty points are the superconducting transition temperatures T_C , and the filled points are the magnetic transition temperatures T_g (in the spin glass phase), and T_N (in the antiferromagnetic phase)

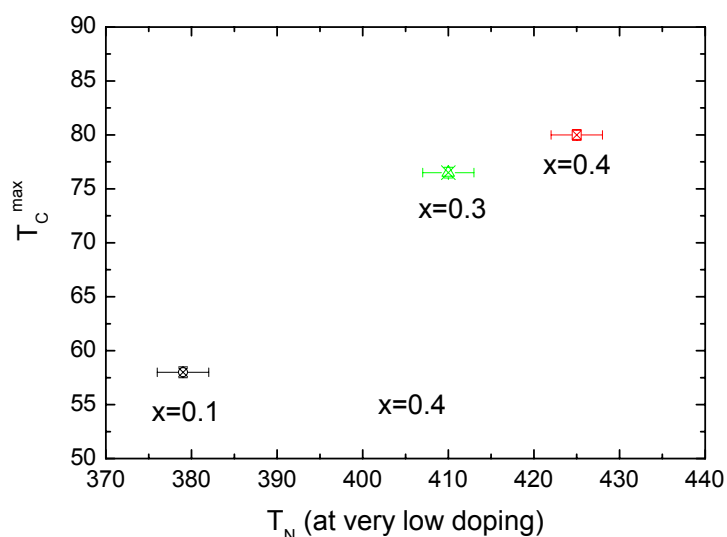


Figure 6-3: The superconducting transition temperature at optimal doping T_C^{\max} as a function of the antiferromagnetic transition temperature T_N for the CLBLCO system.

Chapter 7

SUMMARY

From NQR measurements on YBCO samples with various doping levels, we learned that the resonance frequency of the Cu ions in the planes is proportional to T_C . Since this frequency is proportional to the charges around the nucleus, we conclude that for YBCO the changes in T_C are proportional to the changes in the superfluid density and therefore J_f is a constant for this family of HTSC.

From ZF μ SR performed on undoped CLBLCO samples we determined the magnetic transition temperature and constructed the magnetic phase diagram of the CLBLCO system. We concluded that the family with higher T_N at very low doping, and therefore stronger magnetic interactions and higher J , has indeed a higher T_C^{max} . This confirms the belief that the energy scale J_f is the same for both the superconducting and the antiferromagnetic interactions in the cuprates, and that J_f varies between families but is unique for each family, as suggested in [2].

Appendix A

The derivation of the NQR Hamiltonian

The interaction energy of a charge density $\rho(r)$ with an electric potential V is:

$$E = \int \rho(r)V(r)dr . \quad (\text{A.1})$$

Expanding $V(r)$ in a Taylor series and substituting it into (A.1) yields:

$$E = V(0) \int \rho dr + \sum_{\alpha} V_{\alpha} \int r_{\alpha} \rho dr + \frac{1}{2} \sum_{\alpha, \beta} V_{\alpha, \beta} \int r_{\alpha} r_{\beta} \rho dr \quad (\text{A.2})$$

where

$$V_{\alpha} = \left. \frac{\partial V}{\partial r_{\alpha}} \right|_{r=0} \quad V_{\alpha\beta} = \left. \frac{\partial^2 V}{\partial r_{\alpha} \partial r_{\beta}} \right|_{r=0} .$$

Since the nucleus is the center of mass, the first term is the electric monopole, the electrostatic energy of the nucleus. The second term is the interaction of the electric dipole moment of the nucleus with the electric field. This term vanishes since in the center of mass frame the electric dipole moment is zero. The third term is the quadruple interaction. $V_{\alpha\beta}$ is called the Electric Field Gradient (EFG) tensor.

The EFG

In the quadrupole interaction the environment is taken into account by the EFG. The EFG reflects the asymmetry in the nucleus environment.

The principal axes can always be chosen so that $V_{\alpha\beta}=0$ for $\alpha \neq \beta$ so a diagonal EFG tensor can be written:

$$V = \begin{pmatrix} V_{XX} & 0 & 0 \\ 0 & V_{YY} & 0 \\ 0 & 0 & V_{ZZ} \end{pmatrix} \quad \text{the directions are defined by: } |V_{XX}| \leq |V_{YY}| \leq |V_{ZZ}|$$

From the Laplace equation: $\nabla^2 V = 0 \Rightarrow V_{XX} + V_{YY} + V_{ZZ} = 0 .$

Therefore the number of parameters can be reduced and the EFG tensor can be written as:

$$V = eq \begin{pmatrix} -\frac{1-\eta}{2} & 0 & 0 \\ 0 & -\frac{1+\eta}{2} & 0 \\ 0 & 0 & 1 \end{pmatrix}. \quad (\text{A.3})$$

where: $eq = V_{zz}$ and $\eta = \frac{V_{yy} - V_{xx}}{V_{zz}}$ is the asymmetry parameter

The quadrupole tensor of the nucleus

The quadrupole tensor is defined as:

$$Q_{\alpha\beta} = \int (3r_{\alpha}r_{\beta} - \delta_{\alpha\beta}r^2) \rho dr \quad (\text{A.4})$$

and so the quadrupole energy can be written as

$$E_q = \frac{1}{6} \sum_{\alpha,\beta} V_{\alpha\beta} Q_{\alpha\beta}, \quad (\text{A.5})$$

since the term $V_{\alpha\beta} \delta_{\alpha\beta} \int r^2 \rho dr$ is zero from the Laplace equation.

Quantum mechanical treatment

For a quantum mechanical expression we replace the charge density ρ with the operator $\rho^{(op)}(r) = e \sum_k \delta(r - r_k)$ k – proton number

and hence $Q_{\alpha,\beta}^{(op)} = e \sum_k (3r_{\alpha k} r_{\beta k} - \delta_{\alpha\beta} r_k^2)$.

and the Hamiltonian:

$$H_q = \frac{1}{6} \sum_{\alpha,\beta} V_{\alpha\beta} Q_{\alpha\beta}^{(op)}. \quad (\text{A.6})$$

The eigenstates of the nucleus are characterized by the total angular momentum I of each state, $2I+1$ values of the z component of the angular momentum, and a set of other quantum number ζ . Since we are only interested in the spatial reorientation of the nucleus for a given nuclear energy state, we only need the matrix elements diagonal in both I and ζ :

$$\langle IM\zeta | Q_{\alpha\beta}^{(op)} | IM'\zeta \rangle. \quad (A.7)$$

This expression contains the matrix elements of the coordinates operators. Since for each nucleus its location is connected to its orbital angular momentum, for example: $l_x = \frac{1}{i} \left(y \frac{d}{dz} - z \frac{d}{dy} \right)$, we can convert the coordinates operators to the angular momentum operators. x, y, z refer to the principal directions of the EFG.

I_x, I_y, I_z are the operators of the total angular momentum of the nucleus:

$I_x = \sum_k l_{xk} + S_{xk}$ etc... where l_{xk} and S_{xk} are the x components of the orbital and spin angular momentum of the k -th nucleon.

We now use the irreducible tensor operators T_{2M} [20]. Since the term $3r_{\alpha k} r_{\beta k} - \delta_{\alpha\beta} r_k^2$ is a linear combination of these operators, We replace the coordinates operators with the angular momentum operators, by replacing $(x+iy)$ with I^+ , $(x-iy)$ with I^- and z with I_z , to get the T_{2M} constructed from I^+ , I^- and I_z .

We now use the Wigner-Eckhart theorem [21] that states:

$$\langle IM\zeta | T_{LM} | I'M'\zeta' \rangle = C \langle I\zeta | T_L | I'\zeta' \rangle \quad (A.8)$$

where C is a constant.

It can be shown [19] that using this theorem we obtain:

$$\langle IM\zeta | e \sum_k (3r_{\alpha k} r_{\beta k} - \delta_{\alpha\beta} r_k^2) | IM'\zeta \rangle = C \langle IM\zeta | 3 \frac{(I_\alpha I_\beta + I_\beta I_\alpha)}{2} - \delta_{\alpha\beta} I^2 | IM'\zeta \rangle. \quad (A.9)$$

so the Hamiltonian can be written as:

$$H_q = \frac{\hbar v_q}{6} [3I_z^2 - I^2 + \eta(I_x^2 - I_y^2)]. \quad (A.10)$$

where:

$$v_q \equiv \frac{3e^2 q Q}{2I(2I-1)\hbar} \quad eq = V_{zz}$$

and the quadrupole moment of the nucleus is: $Q = \frac{1}{e} \langle I, m | \sum_k 3Z_k^2 - r_k^2 | I, m \rangle$.

For a nucleus with spin $I=3/2$ the eigenstates and eigenvalues of H_Q are:

$$|1\rangle = a|3/2\rangle + b|-1/2\rangle \quad |2\rangle = a|-3/2\rangle + b|1/2\rangle \quad (\text{A.11})$$

$$|3\rangle = a|-1/2\rangle - b|3/2\rangle \quad |4\rangle = a|1/2\rangle - b|-3/2\rangle$$

$$a^2 + b^2 = 1, a^2 - b^2 = (1 + \eta^2/3)^{-1/2}$$

$$E_{1,2} = (\omega_0/2)(1 + \eta^2/3)^{1/2} \quad E_{3,4} = -(\omega_0/2)(1 + \eta^2/3)^{1/2} \quad (\text{A.12})$$

in this representation H_Q has the form of:

$$H_Q = 2\pi\nu_{NQR} \begin{pmatrix} 1 & 0 & 0 & 0 \\ 0 & 1 & 0 & 0 \\ 0 & 0 & -1 & 0 \\ 0 & 0 & 0 & -1 \end{pmatrix}. \quad (\text{A.13})$$

Where $2\pi\nu_{NQR} = \omega_0(1 + \eta^2/3)^{-1/2}$ is the resonance frequency.

So the system is composed of two doublets of the energy.

Interaction with an external time dependent magnetic field

In the NQR experiment a linearly polarized magnetic rf field is applied with amplitude: $B_1 = \omega_R/\gamma$ and with angles θ, ϕ with respect to the principal axes of the EFG. This adds a time dependent term to the Hamiltonian:

$$H_{rf} = \omega_R \cos(\omega t) [I_X \sin \theta \cos \phi + I_Y \sin \theta \sin \phi + I_Z \cos \theta]. \quad (\text{A.14})$$

This term adds nonvanishing matrix elements with $|\Delta m|=1$, so it can produce resonant transitions between the quadrupole levels.

References

- [1] Y. J. Uemura *et al.*, Phys. Rev. Lett. **62**, 2317 (1989).
- [2] A. Kanigel, A. Keren, Y. Eckstein, A. Knizhnik, J. S. Lord, A. Amato., Phys. Rev. Lett **88**,137003 (2002).
- [3] J.M. Tranquada *et al.*, Phys. Rev. Lett. **60**, 156 (1988).
- [4] F .C. Zhang and T. M. Rice, Phys. Rev. **B37**, 3759 (1988).
- [5] D. Goldschimt *et al.*, Phys. Rev. B **48**, 532 (1993).
- [6] O. Chmaissem, Y. Eckstein, C.G. Kuper, Phys. Rev. B **63**, 174510 (2001).
- [7] A. Knizhnik *et al.*, Physica C **321**, 199 (1999).
- [8] A. Keren, A. Kanigel, J. Lord, A. Amato, Solid State Comm. 126, 39-46 (2003).
- [9] E.H. Brandt, Phys. Rev. B **37**, 2349 (1987).
- [10] M. Tinkham, Introduction to Superconductivity, McGraw-Hill, 1975.
- [11] A. J. Vega, Israel Journal of Chemistry **32**, 195 (1992).
- [12] S. J. Blundell, cond-mat / 0207699 (2002).
- [13] A. Knizhnik, Journal of Physics and Chemistry of solids **64**, 273 (2003).
- [14] A. J. Vega, W. E. Farneth, E. M. McCarron and R. K. Bordia, Phys. Rev. B **39**, 2322 (1989).
- [15] H. Yasuoka, T. Shimiza, Y. Ueda and K. Kosuge, Journal of the Physical Society of Japan **57**, 2659 (1988).
- [16] C.H. Pennington, D.J. Durand, D.B. Zax, C.P. Slichter, J.P. Rice, D.M. Ginsberg, Phys. Rev. B **37**, 7944 (1988).
- [17] H. Lutgemeier, Physica C **153**, 95 (1988).
- [18] J. Haase, O.P. Sushkov, P. Horsch and G.V.M. Williams, Phys. Rev. B **69**, 094504 (2004).
- [19] A.T.Fiory *et. al.*, Phys. Rev. Lett. **65** , 3441 (1990)
- [20] C.P. Slichter, Principles of Magnetic Resonance, Third edition. Springer-Verlag, 1990.
- [21] C.C. Tannoudji, B. Diu and F. Laloe, Quantum Mechanics, Vol 2, page 1048.

תלות בין הטמפרטורה הקריטית של מוליכי על
נחשתניים לבין חוזק
האינטראקציה המגנטית שלהם

רינת אסא

**תלות בין הטמפרטורה הקריטית של מוליכי על נחושתניים
לבין חוזק
האינטראקציה המגנטית שלהם**

חיבור על מחקר

לשם מילוי חלקי של הדרישות לקבלת התואר
מגיסטר למדעים בפיסיקה

רינת אסא

הוגש לסנט הטכניון - מכון טכנולוגי לישראל
סיון תשס"ד חיפה מאי 2004

המחקר נעשה בהנחיית פרופ, עמית קרן בפקולטה לפיסיקה בטכניון

אני מודה לפרופ' עמית קרן על ההנחיה המעולה ועל כל העזרה והתמיכה.

אני מודה לטכנאי המעבדה: גלינה בזליצקי, ד"ר לאוניד יומין ולריסה פתלגן על כל העזרה.

אני מודה לכל חבריי בקבוצת המחקר: אורן, אווה, אושרי, מני אריאל וליאור ותודה מיוחדת לשחר ועמית על העזרה הרבה.

אני מודה לטכניון על התמיכה הכספית הנדיבה בהשתלמותי

להורי, דניאל ועדי על האהבה והתמיכה ללא סייג

ולאורן, על הכל.

תוכן עניינים

ix	תקציר באנגלית
1	רשימת סמלים
3	1 הקדמה
7	2 חומרים – מבנה ותכונות
7	2.1 YBCO
9	2.2 CLCLCO
11	3 סקירה של עבודות קודמות
11	3.1 הקשר של יומורה
12	3.2 יחסי סילום
15	4 שיטות ניסיוניות
15	4.1 תהודה קוודרופולית מגנטית
17	4.1.1 רצף הד ספיני
18	4.1.2 תנאי הניסוי
19	4.2 μ SR
19	4.2.1 הפקת מיואנים, השתלה בגדם ודעיכה
20	4.2.2 תצורה ניסיונית
23	4.2.3 מיואנים בחומר ללא שדה חיצוני
24	4.3 הכנת דגמים
26	4.3.1 אוריינטציה
26	4.3.2 דגמים מועשרים
27	5 תוצאות
27	5.1 תהודה קוודרופולית מגנטית על YBCO
32	5.2 μ SR על CLBLCO

35	6	דין
35	6.1	תהודה קוודרופולית מגנטית על YBCO.....
38	6.2	SR על CLBLCO.....
41	7	סיכום
43	A	פיתוח ההמילטוניאן של תהודה קוודרופולית מגנטית
47		רשימת מקורות
ט		תקציר

רשימת איורים

4	מאפיינים עיקריים של דיאגרמת פאזות של קופרטים.....	1.1
8	דיאגרמת פאזות של YBCO.....	2.1
8	תא יחידה של YBCO.....	2.2
	השתנות T_C עם סימום בחמצן ב CLBLCO עבור ערכים שונים של x . נלקח מ	2.3
9	[8].....	
	דיאגרמת ימורה: T_C כנגד רוחב הקו של המיזאון σ בניסוי μ SR עבור	3.1
	משפחות CLBLCO, YBCO ו LSCO. σ פרופורציוני ל λ^2 שפרופורציוני ל	
12	n_g/m^* . λ הוא עומק החדירה המגנטי [3].....	
	(a) T_C/T_C^{max} ו (b) T_g/T_C^{max} כפונקציה של $\Delta\rho=K_f\Delta y$ עבור מספר משפחות	3.2
	של על מוליכים בטמפרטורה גבוהה. K_f נבחר כך ש T_C/T_C^{max} כנגד $\Delta\rho$ עבור	
	משפחות שונות של קופרטים יקרוסו לעקומה אחת. כתוצאה מכך T_g/T_C^{max} גם	
14	כן קורס לעקומה אחת.....	
	תצורה שונה של גרעין אליפטי בשדה של ארבעה מטענים. התצורה (b) עדיפה	4.1
15	מבחינה אנרגטית.....	
	תיאור סכמטי של רצף הד ספיני. אחרי שני הפולסים מופיע הד גאוסיאני.	4.2
18	הפולריזציה הסכמטית המתוארת למטה היא ל NMR על ספין 1/2.....	
20	התפלגות זוויתית של הפוזיטרונים הנפלטים בתהליך הדעיכה של המיזאון.....	4.3
22	איור סכמטי של ניסוי μ SR.....	4.4
	(a) מספר הפוזיטרונים שנקלטו בגלאי הקדמי והאחורי כתלות בזמן. (b)	4.5
23	פונקצית האסימטריה של המיזאון.....	
24	פרסציה של ספין המיזאון סביב שדה מגנטי בזווית θ	4.6
	פולריזצית Kubo-Toyabe, הדעיכה של ספין המיזאון אודות להתפלגות שדות	4.7
25	גאוסיאנית.....	
	תהודה קוודרופולית מגנטית בסחיפת תדר על דגמי YBCO. הקווים המנוקדים	5.1
	הם התוצאות הניסיוניות. הקווים החלקים הם התאמה לגאוסיאן שנעשתה על	
28	מנת לקבוע את תדירות הרזוננס.....	

5.2	תהודה קוודרופולית מגנטית בסחיפת תדר עבור $YBCO_7$ עם שני האיזוטופים של הנחושת. במקום תדירות רזוננס בודדת יש שתי תדירויות עבור Cu^{65} ו Cu^{63}	28
5.3	יחס העוצמות בין הקו של 29MHz ו 31MHz כפונקציה של הסימון. ככל שרמת הסימון יורדת והחמצן מוצא מהשרשרות, עוצמת הקו של $Cu(2)$ עם שרשרת חצי מלאה (29MHz) עולה על חשבון הקו של $Cu(2)$ עם שרשרת מלאה (31MHz).....	29
5.4	דרגת סימון החמצן ב $YBCO$ כתלות בתדירות תהודה קוודרופולית מגנטית....	30
5.5	איור סכמטי של אתרי הנחושת עם קורדינציה שונה של אטומי חמצן.....	31
5.6	עקומי אסימטריה לטמפרטורות שונות עבור ארבעה דגמי CLBLCO.....	33
5.7	האמפליטודה של הפאזה המגנטית A_m כתלות בטמפרטורה עבור דגם עם $x=0.4$ ו $y=6.607$	33
6.1	T_C של דגמי $YBCO$ שונים כתלות בתדירות תהודה קוודרופולית מגנטית. הקווים הרציפים הם התאמה של התוצאות לשלושה קווים בעלי שיפוע משותף.	36
6.2	T_C, T_g ו- T_N כתלות בסימון החמצן עבור ארבע משפחות של CLBLCO. הנקודות החלולות הן טמפרטורת המעבר המגנטית T_C . הנקודות המלאות הן טמפרטורת המעבר של הפאזה המגנטית T_g (בפאזה הספינית הזכוכיתית) ו- T_N (בפאזה האנטיפרומגנטית).....	39
6.3	$-T_C^{max}$ טמפרטורת המעבר לעל מוליך בסימון אופטימלי, כתלות ב $-T_N$ טמפרטורת המעבר לאנטיפרומגנט עבור מערכת ה CLBLCO.....	39

תקציר

מוליכי העל הנחושתיים הם תרכובות קרמיות המכילות מישורים של נחושת וחמצן, הניתנים לסימום על ידי הכנסת חורים טעונים. הכנסת החורים מתבצעת ע"י החלפת אטומים מחוץ למישורים באטומים אחרים בעלי מספר שונה של אלקטרונים ברמה החיצונית. ניתן להסתכל על חומרים אלה כתלות ברמת הסימום: ברמות סימום נמוכות מאוד חומרים אלה הם מבודדים אנטיפרומגנטים. עם עליית רמת הסימום, טמפרטורת המעבר למצב אנטיפרוטומגנט T_N יורדת מהר מאוד, עד שברמת סימום של בערך 4% אין יותר סדר מגנטי לטווח ארוך. מעל רמת סימום מסוימת מופיעה העל מוליכות. טמפרטורת המעבר למצב על מוליך T_C עולה עם הסימום עד לרמה של סימום אופטימלי שבו טמפרטורת המעבר היא מקסימלית T_C^{max} . סימום נוסף מעבר לרמה זו גורם לירידה ב T_C . באזור בדיאגרמת הפאזות שבו אין יותר סדר מגנטי לטווח ארוך ועד לאזור שבו מתחילה העל מוליכות ישנו סידור אקראי קפוא של המומנטים המגנטיים מתחת לטמפרטורת הקיפאון T_g . זוהי הפאזה הזכוכיתית הספינית (spin glass), פאזה זו קיימת גם בדגמים על מוליכים בסימום נמוך. עבודה קודמת שנעשתה בקבוצה שלנו [2] בדקה את הקשר שבין T_g ו- T_C^{max} .

עבודות אלה הדגימו שבעל מוליכים הנחושתיים מתקיים הקשר:

$$T_C \propto J_f n_s$$

כאשר J_f הוא קבוע הצימוד של היזנברג (לאינטראקציה מגנטית) עבור משפחה של על מוליכים ו- n_s היא צפיפות נושאי המטען העל מוליך. למרות זאת לא נמצא עד כה אישור ניסיוני ברור לכך ש J_f הוא קבוע למשפחה נתונה או לכך שיש קורלציה בין T_C^{max} טמפרטורת המעבר לעל מוליך ברמת סימום אופטימלית, לבין T_N טמפרטורת המעבר לאנטיפרומגנט.

החלק הראשון של העבודה מתמקד באישוש ההנחה שסקלת האנרגיה J_f היא יחודית לכל משפחה של על מוליכים נחושתיים, והיא קבועה בכל רמות הסימום במשפחה. לשם כך ביצעתי מדידות בתהודה קוודרופולית גרעינית [NQR]. שיטת מדידה זו עובדת על גרעינים שהתפלגות המטען בהם אינה ספרית, כגון גרעין הנחושת בעל ספין 3/2. בגרעינים אלה מומנט הקוודרופול החשמלי של המטענים הסובבים את הגרעין גורם ליצירת שתי רמות אנרגיה לגרעין. ההפרש בין רמות האנרגיה נקבע על ידי הנגזרות השניות של השדה החשמלי של המטענים הסובבים את הגרעין [EFG]. בניסוי NQR מודדים את תדר התהודה

למעבר בין רמות האנרגיה. המדידה מתבצעת ע"י הפעלת שני פולסים באורך $t_{\pi/2}$ ו- $2t_{\pi/2}$ של זרם חילופין בתדירות RF עם זמן τ בין הפולסים. הפולסים משודרים לסליל שבתוכו נמצא הדגם ויוצרים שדה בכיוון הציר של הסליל. כאשר תדירות השידור מתאימה לתדירות הרזוננס למעבר בין רמות האנרגיה, נוצר הד בסליל לאחר זמן τ , הנמדד במערכת ע"י קביעת המתח בסליל.

הניסוי בוצע על דגמי YBCO ברמות סימון שונות ומכאן בטמפרטורות מעבר T_C שונות. ב-YBCO, מלבד המישורים של Cu-O, ישנן גם שרשראות חד ממידיות של Cu-O. הסימון ב YBCO נעשה ע"י הוספת חמצן לשרשראות שגורמת לעליה במספר החורים במישורים. מדידת תדרי ה NQR של הנחושת במישורים הראתה כי ב $YBCO_7$ ישנו תדר אחד ב 31.5MHz, שעל פי ניסויים קודמים [14] מתאים לנחושת במישור כאשר השרשרות מלאות בחמצנים. ככל שיוורדים ברמת הסימון מופיעים עוד תדרי רזוננס שמתאימים לנחושת במישור עם סביבה יונית שונה. בסך הכל קיבלנו שלושה סוגים של תדרי רזוננס המתאימים לנחושת במישור עם שלוש סביבות יוניות שונות (תמונה 4-5): תדר ב- 31.5MHz מתאים לסביבה של שרשראות מלאות, תדר של 29MHz מתאים לסביבה של שרשרות חצי מלאות ותדר של 27.5MHz המתאים לסביבה של שרשרות ריקות. כל אחד מסוגי תדרי הרזוננס משתנה בהדרגה ככל שיוורדים ברמת הסימון עקב שינוי במספר החורים במישורים (תמונה 1-6). בשרטוט של תלות השינוי בתדירות ה NQR בכל אחת מהסביבות בטמפרטורת המעבר לעל מוליך T_C מתקבל קשר לינארי, כלומר:

$$T_C \propto \Delta \nu$$

v - תדר ה NQR פרופורציונאלי לצפיפות נושאי המטען ולכן:

$$T_C \propto n_s$$

$$T_C \propto J_f n_s \quad \text{בשילוב ההנחה ש}$$

מתקבל כי עבור משפחת ה YBCO, J_f הוא קבוע בכל דרגות הסימון.

החלק השני של העבודה עוסק את בקורלציה בין T_C ברמת סימון אופטימלית ו- T_N ברמת סימון נמוכה מאוד, עבור משפחה נתונה. למטרה זו השתמשתי במערכת העל מוליכים: $(Ca_x La_{1-x})(Ba_{1.75-x} La_{0.25+x})Cu_3O_y$ (CLBLCO). מערכת זו יציבה לאורך כל העקומה של T_C . כמו כן היא מאפשרת גמישות רבה בבחירת הדגמים, לדוגמה עבור ערכים שונים של ריכוז ה Ca ניתן לקבל, על ידי שינוי בריכוז החמצן, קשתות מקבילות של T_C . המדידות בעבודה זו נעשו בתחום של רמות סימון נמוכות, בהן הדגמים אינם על מוליכים. כל x שונה מהווה משפחה שונה של על מוליכים בעלת J_f שונה.

בחלק זה המדידות נעשו בעזרת μSR (דעיכה של ספין המיואון). בשיטה זו מיואונים מוחדרים לתוך הדגם, כך שהספין של כל המיואונים מקוטב באותו כיוון, בניגוד לכיוון התנועה של האלומה. ברגע שהמיואון עוצר בתוך הדגם הספין שלו מבצע פרסציה סביב השדה המגנטי המקומי שהוא חש, כאשר תדר הסיבוב נקבע על פי גודל השדה. זמן החיים של המיואון הוא כ- $2.2\mu\text{sec}$, הוא דועך לפוזיטרון ושני ניוטרינו. עקב אי-הסימטריה של הכח החלש הפוזיטרון נפלט בעדיפות בכיוון הספין של המיואון ברגע הדעיכה. הדגם מוקף במספר גלאי פוזיטרונים שמאפשרים לעקוב אחר הקיטוב הממוצע של המיואונים כתלות בזמן, ומכאן לשחזר את התפלגות השדה המגנטי בתוך הדגם.

בטמפרטורות גבוהות התפלגות השדה בדגמים שלנו ניתנת להסבר על ידי התפלגות המומנטים הגרעיניים בחומר. בטמפרטורה מסויימת מתרחש שינוי בצורת הדעיכה של המיואון וניתן לזהות שתי תרומות לדעיכה של הקיטוב, רלקסציה מהירה וחלק נוסף של הרלקסציה הגרעינית. ככל שמקררים את הדגם משרעת החלק המהיר גדלה על חשבון החלק האיטי של הרלקסציה הגרעינית. טמפרטורת המעבר הוגדרה כנקודה בה משרעת החלק המגנטי (המהיר) שווה למחצית הקיטוב ההתחלתי של המיואון. סוג טמפרטורת המעבר תלוי ברמת הסימון של הדגם: T_g – ברמות סימון בהן אין סדר מגנטי בטווח ארוך ו T_N – ברמות הסימון הנמוכות בהן יש סדר אנטיפרומגנטי ארוך טווח. מדידות אלה מאפשרות לבנות את דיאגרמת הפאזות עבור מערכת ה-CLBLCO.

מדידות קודמות שנעשו [2] בתחום העל מוליך הראו כי למשפחה בעלת T_C^{max} הגבוה יותר יש טמפרטורת מעבר לפאזה הספינית הזכוכיתית T_g נמוכה יותר. בתחום זה התלות של T_g ב J_f , קבוע הצימוד של היזנברג הוא:

$$T_g = J_f \cdot f(\Delta p)$$

כאשר $f(\Delta p)$ היא פונקציה מורכבת של רמת הסימון. בגלל מורכבות פונקציה זו לא ניתן ללמוד מתוך T_g על החוזק של J_f . לכן בעבודה זו המשכתי את דיאגרמת הפאזות לתחום האנטיפרומגנט, בו הקשר בין T_g ו J_f הוא פשוט.

דיאגרמת פאזות זו מראה כי המשפחה בעלת טמפרטורת מעבר לעל מוליך בסימון אופטימלי T_C^{max} גדולה יותר, ולכן גם J_f גדול יותר, היא גם המשפחה בעלת טמפרטורת מעבר לאנטיפרומגנט T_N גדולה יותר (תמונה 2-6).

תוצאות אלה מחזקות את ההנחה שבעל מוליכים הנחושתיים סקלת האנרגיה J_f זהה

עבור האינטראקציה העל מוליכה והאינטראקציה האנטיפרומגנטית. כמו כן העובדה ש T_C^{max} היא פונקציה מונוטונית עולה של T_N מלמדת על כך שהסיבה להבדל ב T_C^{max} בין המשפחות השונות של CLBLCO נובע שהבדל ב J_f בין המשפחות ולא בהבדל במספר נושאי המטען בסימון אופטימלי.